Sensitivities of Ozone and Radiative Forcing to Supersonic Aircraft Emissions Across Two Flight Corridors

van 't Hoff, Jurriaan A.; Grewe, Volker; Dedoussi, Irene C.

DOI
10.1029/2023JD040476

Publication date
2024

Document Version
Final published version

Published in
Journal of Geophysical Research: Atmospheres

JGR Atmospheres

RESEARCH ARTICLE
10.1029/2023JD040476

Sensitivities of Ozone and Radiative Forcing to Supersonic Aircraft Emissions Across Two Flight Corridors

Jurriaan A. van 't Hoff[1], Volker Grewe[1,2], and Irene C. Dedoussi[1,3]

[1]Faculty of Aerospace Engineering, Section Aircraft Noise and Climate Effects, Delft University of Technology, Delft, The Netherlands, [2]Institut für Physik der Atmosphäre, Deutsches Zentrum für Luft- und Raumfahrt, Weßling, Germany, [3]Department of Engineering, University of Cambridge, Cambridge, UK

Key Points:

- NO_x emissions are the main driver of global ozone loss and the climate impact of supersonic emissions
- Supersonic emissions above the Arabian sea have almost twice the ozone and radiative forcing (RF) impact of equivalent over the Atlantic
- Second-order interactions between NO_x, SO_x, and H_2O emissions affect ozone depletion and RF, albeit at a small scale

Supporting Information:

Supporting Information may be found in the online version of this article.

Correspondence to:

I. C. Dedoussi,
i.c.dedoussi@tudelft.nl

Citation:

van 't Hoff, J. A., Grewe, V., & Dedoussi, I. C. (2024). Sensitivities of ozone and radiative forcing to supersonic aircraft emissions across two flight corridors. *Journal of Geophysical Research: Atmospheres*, *129*, e2023JD040476. https://doi.org/10.1029/2023JD040476

Received 29 NOV 2023
Accepted 19 OCT 2024

Abstract Civil supersonic aviation may return in the near future. Their emissions have been found to lead to changes in the composition of the stratosphere, affecting the ozone layer and climate. To keep up with the rapid developments in supersonic aircraft technology and alternative fuels there is an increasing need for the development of surrogate modeling methods, which requires knowledge of the sensitivities to these emissions. We present a parametric study which evaluates the first- and second-order sensitivities of the ozone column and radiative forcing (RF) to supersonic emissions across two flight corridors and three altitudes. For a given increase in global fuel burn, we find that the increase in emission of NO_x is the main driver of both the changes in the global ozone column and RF, the latter of which is linked through changes in the ozone distribution. Followed by the increase in the emission of SO_x, which leads to O_3 loss and has a cooling effect. The ozone column and climate are least sensitive to increases in H_2O emissions. We also show that interactions between NO_x, SO_x, and H_2O emissions lead to non-linear behavior in the atmospheric response. The effect of these interactions can lead to <5% differences in the ozone column impacts and up to 7.3% increases in RF. Our results demonstrate that the majority of second-order sensitivities may be neglected in surrogate models for small errors, which could greatly simplify their development. Our results also indicate that reductions in flight altitude and fleetwide NO_x emissions may effectively reduce the environmental footprint of supersonic aviation emissions.

Plain Language Summary Supersonic civil aircraft may return in the next decade, and their emissions may cause long-term changes to the climate and the ozone layer. To keep up with this rapidly developing sector we need fast surrogate models, which can be incorporated in design optimisation processes. In this work we evaluate how the ozone layer and climate respond to 26 different emission scenarios, to determine the sensitivity to common emission species and the location of emissions. We show that, for an increase in fuel burn, the ozone column and climate are most sensitive to the associated NO_x emissions, followed by SO_x and H_2O. We also show that when two emissions are increased simultaneously, interactions between them lead to a different response than if they were considered individually. These interactions change the ozone response by up to 5%, and the climate response by up to 7.3%. Often their effect is smaller, which implies that we could neglect them to simplify model development.

1. Introduction

Over the past decades the global demand for air transportation has grown considerably, even considering setbacks from the COVID-19 pandemic (Dube, 2023). The rising demand in fast air travel has reinvigorated commercial interest in the use of civil supersonic transport aircraft (SSTs). These aircraft are designed to operate at higher altitudes than subsonic aircraft, with modern concepts ranging between cruise altitudes of 15 and 20 km (Matthes et al., 2022). The increase in cruise altitude enhances the impact of non-CO_2 emissions from SSTs compared to their subsonic counterparts. For example, H_2O emissions are identified as an important driver of the climate impact due to the high stratospheric residence time, and the insertion of emissions into the ozone layer is expected to lead to long-term changes in the global ozone distribution, which also affects global radiative forcing (RF) (Eastham et al., 2022; Grewe et al., 2007; Matthes et al., 2022; Speth et al., 2021; Tuck, 2021; Zhang et al., 2021b, 2023). Changes in the distribution of ozone also pose a risk to public health; the depletion of the global ozone layer is associated with increases in mortality from increased surface exposure to UV radiation (Eastham et al., 2018; McKenzie et al., 2015), and an increase in ozone may negatively affect our air quality and climate (Grewe et al., 2007; Maruhashi et al., 2022; Quadros et al., 2020).

The emission of nitrogen oxides (NO_x, NO + NO_2) is often found to be the main contributor to the global ozone column impact of SST emissions (Fritz et al., 2022; Kawa et al., 1999; Speth et al., 2021; Zhang et al., 2021a, 2021b, 2023). At supersonic cruise altitudes NO_x emissions lead to catalytic ozone destruction in the mid-stratosphere by binding free oxygen, while increasing ozone production in the lower stratosphere and troposphere from the photodissociation of NO_2 (Johnston, 1971; Lin et al., 1988; Matthes et al., 2022; Penner et al., 1999; Tuck, 2021). The changes in the distribution of O_3 affect RF (de F. Forster & Shine, 1997; Iglesias-Suarez et al., 2018), making NO_x emissions an important part of the climate impact of supersonic vehicles. Recent works have found its contribution to RF can exceed that of H_2O emissions (Eastham et al., 2022; Zhang et al., 2021b, 2023).

Second to NO_x are SO_x emissions, which originate from fuel impurities and additives. Sulfur is primarily emitted through gaseous SO_2, which leads to the formation of sulfuric acid (H_2SO_4) aerosols. These aerosols facilitate the heterogeneous conversion of NO_x to nitric acid (HNO_3), suppressing mid-stratospheric ozone loss from the NO_x cycle while also increasing lower-stratospheric ozone loss to ClO_x and HO_x radicals (Brasseur & Granier, 1992; Granier & Brasseur, 1992; Hofmann & Solomon, 1989; Kinnison et al., 2020; Pitari et al., 2014; Solomon, 1999; Tie & Brasseur, 1995). Earlier works have demonstrated that SO_x emissions from SSTs have extensive effects on global ozone composition and RF (Danilin et al., 1997; Eastham et al., 2018; Krishna-Pillai Sukumara-Pillai et al., 2019; Speth et al., 2021; Weisenstein et al., 2021; Zhang et al., 2023).

Ozone is also affected by the emissions of H_2O, which photodissociates to form HO_x. HO_x depletes ozone through the HO_x cycle, which is most effective in the upper stratosphere (Lary, 1997; Tuck, 2021). Compared to the impact of NO_x and SO_x, the ozone impact of H_2O emissions is smaller for supersonic aircraft, but H_2O emissions are often found to be an important contributor to the climate impact (Grewe et al., 2007; Matthes et al., 2022; Speth et al., 2021; Zhang et al., 2021a). These impacts are enhanced at higher emission altitudes, increasing the effect of H_2O emissions for hypersonic vehicles (Kinnison et al., 2020; Pletzer et al., 2022; Pletzer & Grewe, 2024).

Finally, there are several other SST emissions species with smaller effects on ozone and RF that are studied less often, as they either raise little concern or require complex model capabilities. An example of the former is the emission of carbon monoxide (CO) and hydrocarbons (HC), which are considered to have a negligible effect on ozone due to their small emission quantities and indirect effects (Speth et al., 2021). In the latter case, the emission of black carbon (soot) aerosols is expected to accelerate ozone loss through warming of the stratosphere (Maloney et al., 2022; Matthes et al., 2022), the effect of which can only be studied with models capable of capturing this feedback.

Despite the increasing certainty about the role of non-CO_2 emissions from SSTs, these are not yet covered by international regulations (ICAO, 2017). With SSTs still under development, a challenge in engineering, operational, and regulatory decision-making is the feedback that the regulations themselves would impose on potential designs or future SST adoption. The economic viability of SST flight routes and fleet sizes is sensitive to regulations (Speth et al., 2021), meaning that regulations themselves will result in changes in the prospective spatial composition of global fleet emissions, complicating the evaluation of their effectiveness. For example, studies have shown that lower SST cruise altitudes are associated with reductions in ozone depletion (Fritz et al., 2022; Zhang et al., 2021b). However, a lower cruise altitude may come at a cost of increasing the climate impact if the cooling effect from ozone loss is dominant (Grewe, Stenke, et al., 2010), although the opposite has also been found to occur (Zhang et al., 2023). It may also decrease the fleet's fuel efficiency unless the vehicle design is adapted, which may potentially lead to a different global distribution of flights, emissions and, subsequently, atmospheric impacts.

To navigate these feedbacks and trade-offs, an iterative approach with in-the-loop tools is necessary for the evaluation of different impact metrics. This is incompatible with modern methodologies, which evaluate the impacts of SST emissions using chemistry-transport models (CTMs). CTMs can capture intricate atmospheric responses and feedback mechanisms, but this level of detail comes at a considerable computational cost. For example, the decade-long GEOS-Chem models that we ran for this work required over 45 days of consecutive run time with 32 CPUs. These models are unsuitable for in-the-loop applications, therefore we need to develop surrogate models which are still representative of CTM evaluations. A possibility is the use of reduced-order response models, where we first evaluate the impact of a sparse network of SST emission scenarios with a CTM and then use simplified models to interpolate between the CTM evaluations. Previous works have already studied isolated, one-dimensional responses, such as changes in cruise altitudes (Dutta et al., 2004, 2005; Zhang et al., 2021b) and the emission of species such as NO_x (Dutta et al., 2005; Grewe et al., 2007; Grewe, Plohr, et al., 2010; Kawa et al., 1999), or SO_x and H_2O (Fritz et al., 2022; Speth et al., 2021).

The usability of these models is still restricted to one-dimensional cases, such as changes to individual emission indices or the cruise altitude, because they lack the higher-order interactions between these parameters. Since the atmospheric responses are non-linear, these higher-order interactions could be critical for both the in-depth understanding of the underlying chemical processes and the accuracy of the resulting reduced-order models. Adjoint modeling has recently been used to map spatial dependencies of ozone sensitivities to NO_x, H_2O, and SO_x emissions, potentially extending the application to include spatial dimensions, but these models cannot easily estimate the effect of higher-order interactions between emission species (Dedoussi et al., 2024; Fritz et al., 2022; Speth et al., 2021). With this work we aim to fill this gap by using forward-modeling methods to quantify the effect of secondary interactions between the emission of NO_x, SO_x, and H_2O through second-order sensitivities. We use the GEOS-Chem global CTM in a parametric study, using 26 emission scenarios across two flight corridors and three cruise altitudes, to evaluate first- and second-order sensitivities of the global ozone and RF responses to emission characteristics. Through this we aim to understand the role of higher-order interactions and their magnitude, which may inform the development of surrogate models.

2. Methodology

We evaluate the sensitivities of the global ozone response and RF to supersonic aircraft emissions through a parametric study in two flight corridors using the GEOS-Chem CTM. With first-order sensitivities we indicate the response of the global ozone column to changes in individual emission parameters, for example, an increase in NO_x emissions, whereas second-order cross-sensitivities measure the response to two simultaneous changes in the emission scenario. Through the latter we aim to explore the importance of non-linear effects from chemistry which may be important for surrogate modeling.

2.1. Atmospheric Modeling

We use version 13.3.1 of the GEOS-Chem Classic (GCC) model. This version of GEOS-Chem includes the Unified Tropospheric-Stratospheric Chemistry Extension (UCX) module by Eastham et al. (2014) which implements stratospheric chemistry routines using Fast-JX for photolysis reactions (Bian & Prather, 2002). We use a horizontal resolution of $4° \times 5°$ with 72 vertical pressure levels. Global anthropogenic emissions are implemented using version 2 of the Community Emissions Data System (O'Rourke et al., 2021) with subsonic aviation emissions for 2019 from the openAVEM inventory (Quadros et al., 2022). Biomass burning emissions are based on the GFED4 emissions inventory by Giglio et al. (2013). Lightning NO_x emissions are included based on work by Ott et al. (2010) and Murray et al. (2012). Following the benchmark settings of GEOS-Chem, we also rely on several other works for the emission of ethane (Tzompa-Sosa et al., 2017; Xiao et al., 2008), iodocarbons (Ordóñez et al., 2012), bromocarbons (Liang et al., 2010), and anthropogenic particulate matter (Philip et al., 2017). As meteorological input we use the MERRA-2 meteorological re-analysis product by NASA/GMAO (Gelaro et al., 2017). The use of MERRA-2 with a $4° \times 5°$ resolution is reported to lead to excessive horizontal transport (Chabrillat et al., 2018), although Eastham et al. (2022) demonstrated that the mean age-of-air still was within 6 months of reference data (Andrews et al., 2001) at this resolution. While higher horizontal resolutions may improve our results, this was not possible given the large number of evaluations. The consideration of the horizontal resolution is further discussed in Text S2 of Supporting Information S1.

The surface mixing ratios of methane are prescribed by historical data derived from NOAA (Murray, 2016), and similarly surface mixing ratios of other long-lived species such as chlorofluorocarbons are prescribed by historical data sets prepared for the UCX by Eastham et al. (2014). Because we use fixed methane mixing ratios we do not capture the effects of methane feedbacks. Eastham et al. (2022) showed that over several decades of integration methane feedbacks can increase SST-driven O_3 loss by up to 15%, therefore it is likely that we also underestimate O_3 losses. We expect that this underestimation is smaller, as our integration time of 10 years is considerably shorter than the 42 years presented by Eastham et al., and within our timeframe the feedback would not have sufficient time to stabilize (Eastham et al., 2022, Supporting Information S1).

We integrate the impact of the SST emissions over a timeframe of 10 years, using the final 3 years of this integration for analysis. Changes in RF are calculated at the tropopause over this period using the Rapid Radiative Transfer Model for General circulation models (RRTMG) (Heald et al., 2014) with stratospheric adjustment

following the implementation by Eastham et al. (2022). In practice, this is done using version 14.3.1 of the high-performance branch of GEOS-Chem (GCHP), which has the stratospheric adjustment implemented. We apply this model as a post-processing tool by loading the atmospheric states from the GCC v13.3.1 model into GCHP v14.3.1. The cross-compatibility only requires regridding the atmospheric states and neglecting the species not incorporated in GCC v13.3.1, none of which affect global RF. For each atmospheric state we then integrate GCHP with RRTMG for short intervals (3 days), producing snapshots of the atmosphere's RF.

Similar to other studies we quantify the ozone impact through the mean change in global ozone column in Dobson units (DU), which is most closely related to increases in surface UV exposure and subsequently health impacts (Eastham et al., 2022; Fritz et al., 2022; Speth et al., 2021). The 3-year window, also referred to as the analysis period, is chosen following the perturbation-attributable changes in stratospheric OH^-, NO_x, SO_x, and O_3, which stabilize after 7 years of model integration (see Supporting Information S1). Compared to longer timeframes, this is better suited in advent of a rapidly developing near-future SST market, but it limits our capability to evaluate long-term effects such as methane feedbacks (Eastham et al., 2022; Speth et al., 2021). Since input data is not available for the entire 2014–2023 timeframe, we deviate from historical input data after the first of January 2019. After this date we cycle through the 2014–2019 input data again, meaning that the effect of the COVID-19 pandemic on anthropogenic emissions is not incorporated.

Earlier works have evaluated the performance of GEOS-Chem against observations from satellite instruments (TOMAS, OMI, MLS). Comparisons showed that GEOS-Chem UCX can successfully replicate seasonal patterns in global ozone distribution, even within the stratosphere, although it over-estimates the rate at which the seasonal ozone hole recovers (Eastham et al., 2014; Fritz et al., 2022; Speth et al., 2021). We corroborate these findings with a comparison of our simulations with ozone column observations from the TROPOMI instrument (ESA, 2019a; ESA, 2019b) (see Supporting Information S1). Averaged globally, we find that we overestimate global ozone columns by 1.72% with biases of up to 4% at low latitudes and underestimations at high northern latitudes. Seasonal patterns and ozone hole formation are captured well, but the ozone hole recovers earlier in GEOS-Chem compared to the satellite observations.

2.2. Supersonic Aviation Emission Scenarios

We use 26 emission scenarios and an unperturbed baseline scenario. The emission scenarios do not consider a distribution of emissions along complete flight trajectories and are not based on any particular SST concept. Instead, we introduce supersonic emissions as year-round continuous emissions in a cubic volume spanning a single vertical layer of the GEOS-Chem model (height of approximately 1.05 km). These volumes are located over the transatlantic flight corridor (TAC) and the southern Arabian sea (SAS). These regions are chosen for their anticipated use in civil supersonic aviation and their geographic location. The TAC is vital for flights between north America and Europe, and the SAS flight corridor is expected to accommodate an increasing share of SST traffic from growth in the Asian and Arabic markets (Grewe et al., 2007; Kawa et al., 1999; Speth et al., 2021; Zhang et al., 2023). These corridors are also located in different parts of the Brewer-Dobson circulation (Butchart, 2014), which we expect will affect the impact of emissions from these areas.

Figure 1 shows a summary of the emission scenarios, their geographic location, and their annual emissions. We define the TAC region as W53° to W11° and N48° to N57° and the SAS region as E52° to E94° and N15° to N24°. The latter region extends across the Indian mainland, as we prioritize consistency in the emission area over the model grid to ease comparison between the regions. For the altitude of the emissions we consider the altitude domain of expected cruise operation for Mach 1.6 and 2.2 SST concepts (Matthes et al., 2022; Speth et al., 2021), leading to the following altitude bands in GEOS-Chem's vertical grid: 15.73–16.75 km, 17.77–18.80 km, and 19.86–20.92 km. These bands will be referred to using their central altitudes of 16.2, 18.3, and 20.4 km.

We introduce estimated supersonic emissions from 8 Tg of annual fuel burn using generalized SST cruise emission indices based on literature. For NO_x emissions we average the Mach 1.6 and 2.2 vehicle concepts presented by Speth et al. (2021) and the SST concept considered by Zhang et al. (2021a), resulting in an emissions index of 18 g NO_2/kg. Like several other studies, we base H_2O emissions on conventional aviation fuel, resulting in 1.26 kg/kg (Lee et al., 2021; Quadros et al., 2022; Speth et al., 2021; Zhang et al., 2021a, 2023). Similarly, SO_x emissions are also based on modern aviation fuels with sulfur mixing mass ratios of 600 ppm, which we distribute into 98% SO_2 (1.176 g kg^{-1}) and 2% SO_4 (36 μg kg^{-1}) (Eastham et al., 2022; Fritz et al., 2022; Quadros et al., 2022; Simone et al., 2013; Speth et al., 2021). Besides these species we include the emission of carbon monoxide (CO), black

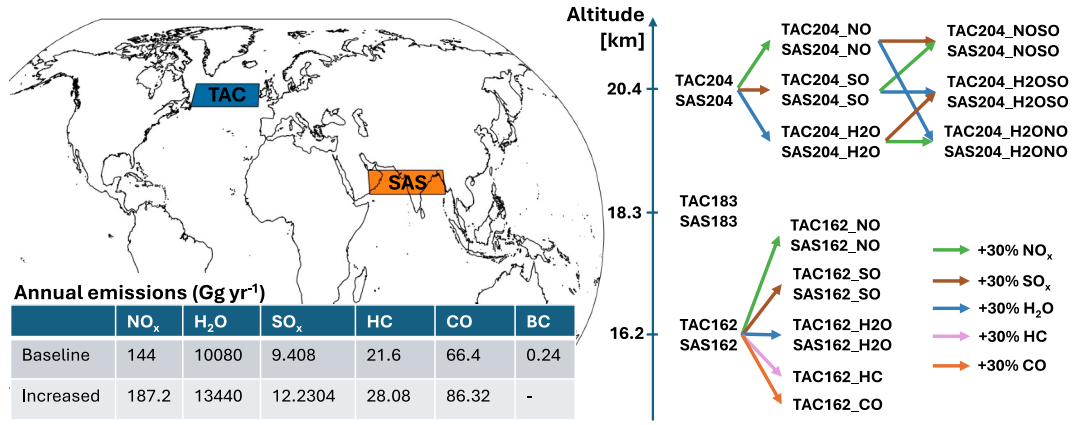

Annual emissions (Gg yr^{-1})

	NO_x	H_2O	SO_x	HC	CO	BC
Baseline	144	10080	9.408	21.6	66.4	0.24
Increased	187.2	13440	12.2304	28.08	86.32	-

Figure 1. Overview of the emission areas and the 26 variations of the emission scenarios. On the left the transatlantic corridor (TAC) and south Arabian sea (SAS) emission areas are shown, as well as a table summarizing the annual emissions for the baseline and increased variations. On the right, we show how the variations of the emission scenarios are connected. Colored arrows indicate increases in specific emissions. Baseline scenarios (e.g., TAC204) use annual baseline emissions, whereas variants increase specific emissions by 30% for the parametric analysis.

carbon (BC), and a collection of hydrocarbons (HC), for which we adopt the average fleet emissions for the 1.8 Mach concept vehicle by Speth et al. (2021), respectively 8.3 g/kg and 2.7 g/kg. HC emissions are split into several species using the same distribution as the openAVEM inventory (Quadros et al., 2022) (see Supporting Information S1).

2.3. Notation and Naming

For the parametric study we use an increase of 30% to the emission indices of one or multiple species. We use a naming convention incorporating the region of the emissions (TAC/SAS), their altitude (162/183/204 for 16.2, 18.3, and 20.4 km respectively), and optionally a suffix to denote species for which the emission is increased by 30%. For example, TAC204 refers to a scenario with emissions in the transatlantic region at an altitude of 20.4 km with the annual baseline emissions as listed in Figure 1. TAC204_NO refers to a variant of this scenario with a 30% increase in NO_x emissions. A table with all emission scenarios and their annual emissions is included in the Supporting Information S1.

We use a simplified notation for ozone and RF sensitivities to the emission species; first-order sensitivities $\left(\frac{\delta O_3}{\delta X}\right)$ are abbreviated as S_X and second-order cross-sensitivities $\left(\frac{\delta^2 O_3}{\delta X \delta Y}\right)$ as S_{X-Y}. Sensitivities are obtained through the attributable differences in ozone columns between scenarios, divided by the corresponding change in species emission mass. For example, the sensitivity to SO_x (S_{SO_x}) is calculated from the TAC204—TAC204_SO scenario pair and cross-sensitivity $S_{NO_x,S}$ is derived by comparing this value with a calculation from the TAC204_NO—TAC204_NOSO pair, in both cases dividing by the corresponding change in annual emissions.

2.4. Fuel Burn Response Estimation

We present a reduced-order response model which estimates the change in column ozone and RF from changes in the emissions using the calculated sensitivities. This model describes a change in ozone column impact or RF (ΔF) as a function of a change in emission altitude Z, and as a series of changes in the annual emission of individual species x, contained within a five-dimensional vector $\vec{X} = (x_1, x_2, x_3, x_4, x_5)$. Here x_i represents changes to the annual emissions of NO_x, SO_x, H_2O, HC, and CO. Earlier work on the sensitivity to altitude by Zhang et al. (2021b) has shown that the response to altitude is non-linear, hence we model the altitude response with a second-order Taylor function using three altitude samples. Other work has also demonstrated the dependency of sensitivities on altitude (Fritz et al., 2022; Matthes et al., 2022; Speth et al., 2021), which we implement through first-order dependency estimations to individual emission species $S_X(Z)$. Here, we use sensitivity calculations at two altitudes to build a linear sensitivity-altitude model. Equation 1 describes the resulting estimate of a change in the ozone impact.

$$\Delta F\left(\vec{X}, Z\right) = Z\left(\frac{\delta O_3}{\delta Z} + \frac{Z}{2}\frac{\delta^2 O_3}{\delta^2 Z}\right) + \sum_{x=1}^{5} x_i \times \frac{\delta F_B}{\delta x_i}(Z) + \epsilon \quad (1)$$

With this estimation, we attempt to condense a complex atmospheric response into a single equation. With estimation error (ϵ) we account for the lack of higher-order terms of the ozone response, such as atmospheric feedbacks and the cross-sensitivities between emission species. We explore this error term using our evaluations of the $S_{NO_x - SO_x}$, $S_{NO_x - H_2O}$, and $S_{NO_x - H_2O}$ cross-sensitivities. These are chosen due to the importance of the associated species to the ozone and RF impacts, as well as their ties through heterogeneous chemistry on sulfate aerosols. We calculate their values at the highest perturbation altitude (20.4 km), where we anticipate these interactions are most influential.

3. Results and Discussion

First, we summarize the effect of the emission scenarios on the global ozone column, stratospheric H_2O, and global RF. Following this, we discuss the first-order sensitivities of the ozone column and climate impacts, and finally we evaluate their second-order cross sensitivities.

3.1. Global Atmospheric Response

Table 1 summarizes the mean changes in global ozone columns, stratospheric H_2O, and RF over the 2021–2023 period for the different scenarios. More detailed tables can be found in the Supporting Information S1. We find that all emission scenarios lead to changes in the global ozone distribution, stratospheric H_2O, and RF, which are described in order over the following subsections.

3.1.1. Changes in Ozone Distribution

Figure 2 shows a comparison of the zonal average changes in global ozone distribution for the 16.2 and 20.4 km emission scenarios in the SAS and TAC regions. The introduction of supersonic aircraft emissions results in increases in lower-stratospheric and tropospheric ozone, coupled with depletion of ozone higher in the stratosphere. The depletion is smaller than the lower-stratospheric increases, resulting in net-increases to global ozone columns in all 16.2 and 18.3 km emission scenarios. Emissions originating in the SAS regions lead to increased upper-stratospheric ozone loss and stronger ozone responses in the southern hemisphere. This can also be seen in Figure 3, which shows the mean seasonal changes in the ozone columns across the four scenarios of Figure 2. Figure 3 shows that the ozone response exhibits different seasonal behavior for each of the emission areas. At 20.4 km altitude emissions from the SAS region lead to consistent loss in column ozone of over 1 DU across the northern hemisphere throughout the year. This varies seasonally for the TAC emissions. At this altitude emissions from the SAS region also enhance the formation of the Antarctic ozone hole and to a lesser extent the Arctic one, whereas TAC emissions only amplify Antarctic ozone hole formation. Emissions from the SAS region have a stronger effect on northern-hemispheric and polar O_3 column depletion. At the altitude of 16.2 km the SAS response is showing a seasonal variation, while the TAC response shows a steady increase in the ozone column over the year.

3.1.2. Changes in Stratospheric H_2O

All emission scenarios lead to increases in stratospheric H_2O, the mass of the perturbation increasing with the emission altitude. The H_2O perturbation lifetime, which is calculated by dividing the stratospheric perturbation mass by the annual emissions (Grewe et al., 2007), also increases with altitude. At 20.4 km the lifetime is considerably stronger for the SAS region, with an average value of 24.6 months compared to 15.5 months in the TAC region. This is likely due to the regions' placements relative to the Brewer-Dobson circulation, as the TAC region lies within downwards transportation pathways whereas the SAS region is closer to tropic upwelling pathways (Butchart, 2014). At lower emission altitudes the perturbation lifetime is smaller for the SAS region however, due to its closer proximity to the tropopause. GEOS-Chem uses fixed tropospheric H_2O mixing ratios, meaning its troposphere acts as a sink for stratospheric H_2O. At 16.2 km the SAS emission region frequently lies within the model tropopause, sharply reducing the stratospheric uptake of H_2O emissions. This results in smaller H_2O perturbation lifetimes for the SAS scenarios at 16.2 and 18.3 km altitude.

Table 1
Summary of Average Impacts From the Emission Scenarios From 2021 to 2023

	Δ H_2O (strat.)		Δ O_3[DU]			Δ RF [mW/m^2]			
	[Tg]	L [months]	Global	SH	NH	Total	O_3	H_2O	Aer.
TAC162	3.00	3.6	0.31	0.09	0.53	2.67	4.00	0.98	−3.27
TAC162_NO	3.03	3.6	0.40	0.12	0.68	4.32	5.17	1.12	−3.26
TAC162_SO	3.00	3.6	0.28	0.08	0.48	1.81	4.00	0.90	−3.95
TAC162_H2O	4.00	3.7	0.31	0.09	0.53	2.92	3.97	1.29	−3.27
TAC162_CO	3.00	3.6	0.31	0.09	0.54	2.64	4.00	0.98	−3.27
TAC162_HC	3.00	3.6	0.31	0.09	0.54	2.67	4.01	0.99	−3.27
TAC183	9.37	11.2	0.14	0.03	0.24	3.91	4.61	2.73	−4.63
TAC204	12.86	15.3	−0.31	−0.02	−0.60	4.16	6.04	3.30	−5.89
TAC204_NO	12.94	15.4	−0.41	−0.00	−0.82	6.22	7.93	3.43	−5.89
TAC204_SO	12.87	15.3	−0.36	−0.04	−0.68	2.68	6.05	3.17	−7.08
TAC204_H2O	17.03	15.6	−0.33	−0.03	−0.64	5.16	5.89	4.39	−5.89
TAC204_NOSO	12.95	15.4	−0.45	−0.02	−0.89	4.75	7.93	3.31	−7.09
TAC204_H2ONO	17.10	15.7	−0.43	−0.01	−0.85	7.21	7.77	4.52	−5.90
TAC204_H2OSO	17.04	15.6	−0.38	−0.04	−0.72	3.97	5.55	4.57	−7.08
SAS162	0.11	0.1	0.29	0.18	0.39	3.11	5.31	−0.10	−2.41
SAS162_NO	0.14	0.2	0.37	0.24	0.50	4.85	6.77	−0.03	−2.41
SAS162_SO	0.11	0.1	0.26	0.17	0.36	2.47	5.32	−0.15	−2.95
SAS162_H2O	0.11	0.1	0.29	0.18	0.39	3.11	5.31	−0.10	−2.41
SAS183	5.25	6.3	0.10	0.07	0.13	3.63	5.52	1.57	−4.62
SAS204	20.49	24.4	−0.70	−0.20	−1.21	7.28	8.55	5.25	−7.33
SAS204_NO	20.65	24.6	−0.89	−0.22	−1.56	10.20	11.15	5.45	−7.36
SAS204_SO	20.51	24.4	−0.76	−0.23	−1.29	5.49	8.57	5.09	−8.82
SAS204_H2O	27.00	24.7	−0.74	−0.22	−1.26	8.79	8.37	6.91	−7.35
SAS204_NOSO	20.67	24.6	−0.94	−0.25	−1.63	8.40	11.16	5.30	−8.84
SAS204_H2ONO	27.17	24.9	−0.92	−0.23	−1.60	11.69	10.96	7.11	−7.37
SAS204_H2OSO	27.03	24.7	−0.79	−0.25	−1.34	6.98	8.40	6.75	−8.85

Note. The H_2O columns contain the stratospheric H_2O perturbation in Tg and the perturbation lifetime (L) in months. The latter is calculated by dividing the perturbation with the annual H_2O emissions. The O_3 columns show the changes in column ozone as global, southern hemispheric (SH), and northern hemispheric (NH) averages. The radiative forcing (RF) columns shows the total change in RF with component contributions of O_3, H_2O, and aerosols (Aer: Black carbon, nitrates, and sulfates).

3.1.3. Changes in RF

Across all scenarios we find increases in RF ranging between 1.81 and 11.69 mW/m^2. Figure 4 summarizes the changes in RF for the SAS204, TAC204, SAS162, and TAC162 scenarios alongside changes attributable to increases in specific emissions. In all scenarios the positive RF from changes in the global O_3 distribution is the largest contributor to the RF impact, matching recent results from Zhang et al. (2023) and Eastham et al. (2022). Second to this is the cooling effect of changes in aerosols (black carbon, nitrates, and sulfates), and third is the warming effect from stratospheric H_2O accumulation. Other contributions are listed in the Supporting Information S1. Figure 4 shows that increases in NO_x emissions also lead to increases in RF due to the warming effect of subsequent changes in the O_3 distribution. Increases in H_2O emissions increase warming from H_2O while slightly reducing that of O_3, and increases in SO_x emissions reduce the net RF by increasing aerosol-driven cooling. Furthermore, we find that changes in CO or HC emissions have negligible effects on RF (Table 1). When multiple emission indices are increased, the individual effects are combined. For example, 30% increases to both NO_x and H_2O result in relative increases in RF of 61% and 73% for the SAS and TAC regions respectively at

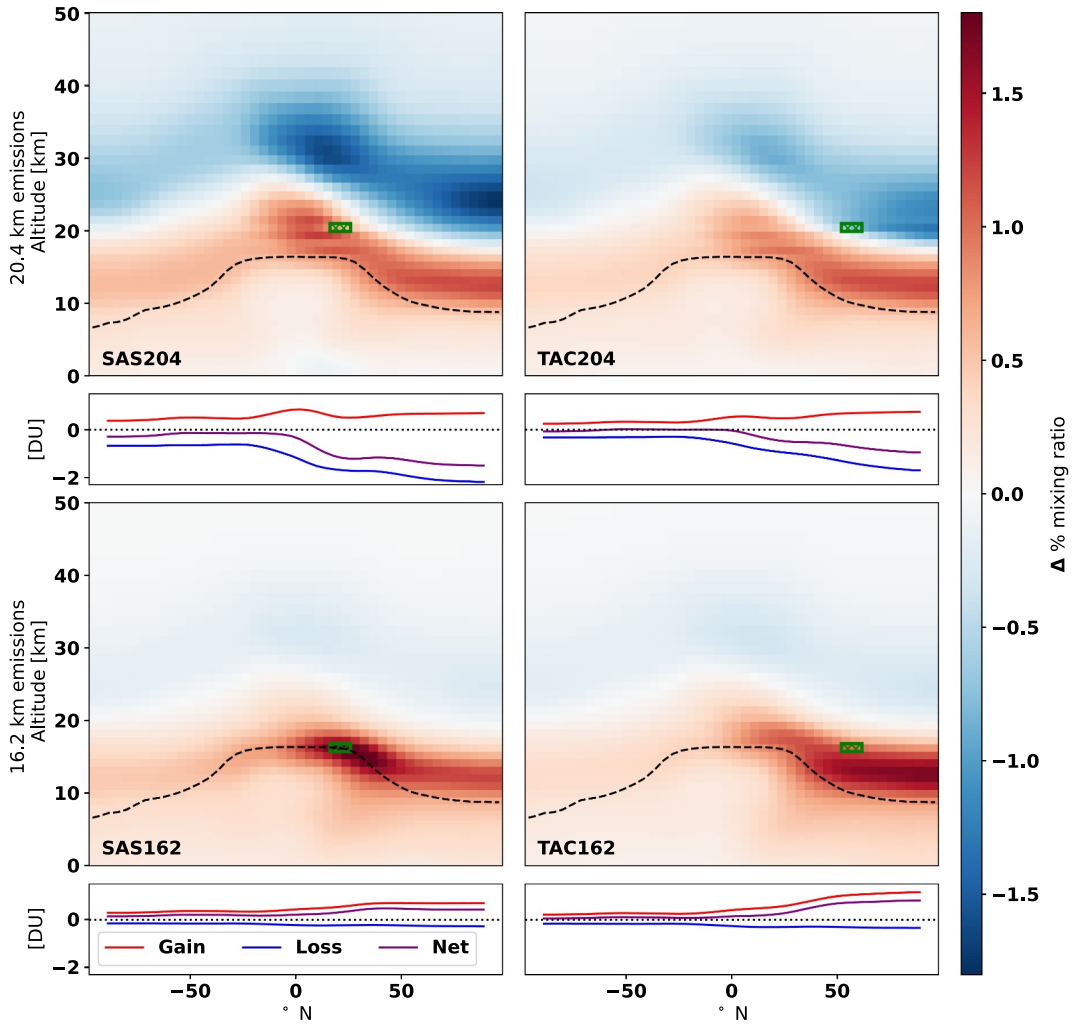

Figure 2. Relative change in ozone mixing ratio between the perturbed simulations (SAS204, TAC204, SAS162, TAC162) and the unperturbed baseline atmosphere (BL). The left column shows the change in response to emissions in the south arabian sea (SAS) flight corridor at 16.2 and 20.4 km (bottom and top row respectively), and the right column shows the equivalent for the transatlantic flight corridor (TAC). Below each zonal average the column ozone gain (red), loss (blue), and net sum (purple) is shown in Dobson units. Green hashed areas indicate the origin of the emissions.

20.4 km altitude. Figure 4 also shows that these simultaneous increases in emissions result in non-linear changes in RF, this is evaluated by comparing the response to two components to a sum of the individual responses. These non-linearities will be discussed in Section 3.3.

3.1.4. Difference Between Emission Regions

All metrics of the atmospheric impact listed in Table 1 are more sensitive to emissions from the SAS region, particularly at higher emission altitudes. We expect that this is driven by this region's position relative to the Brewer-Dobson circulation (Butchart, 2014). Due to the proximity to the tropic pipes the emissions spread to the upper-stratosphere and southern hemisphere faster, enhancing their impacts. This can be observed through the large increases in the southern hemispheric O_3 column responses for the SAS scenario and the increase in H_2O emission lifetime. It can also be observed by comparing the transport of black carbon-like tracers (unaffected by chemistry or deposition), which are included alongside the emissions. When emitted from the SAS region, these travel to the upper-stratosphere within 1.5 years, whereas it takes up to 3 years for TAC emissions (Figure S12 in Supporting Information S1). Over time, this leads to higher accumulation of emissions in the upper-stratosphere, enhancing the

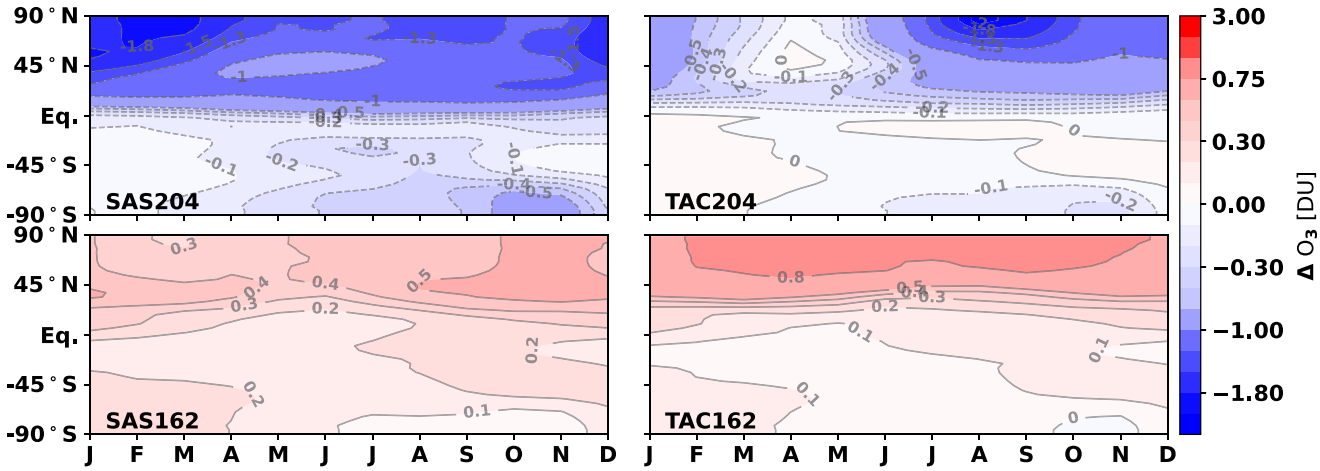

Figure 3. Mean changes in monthly column ozone in response to the SAS204 (top left), TAC204 (top right), SAS162 (bottom left), and TAC162 (bottom right) emission scenarios. Values are shown in Dobson units.

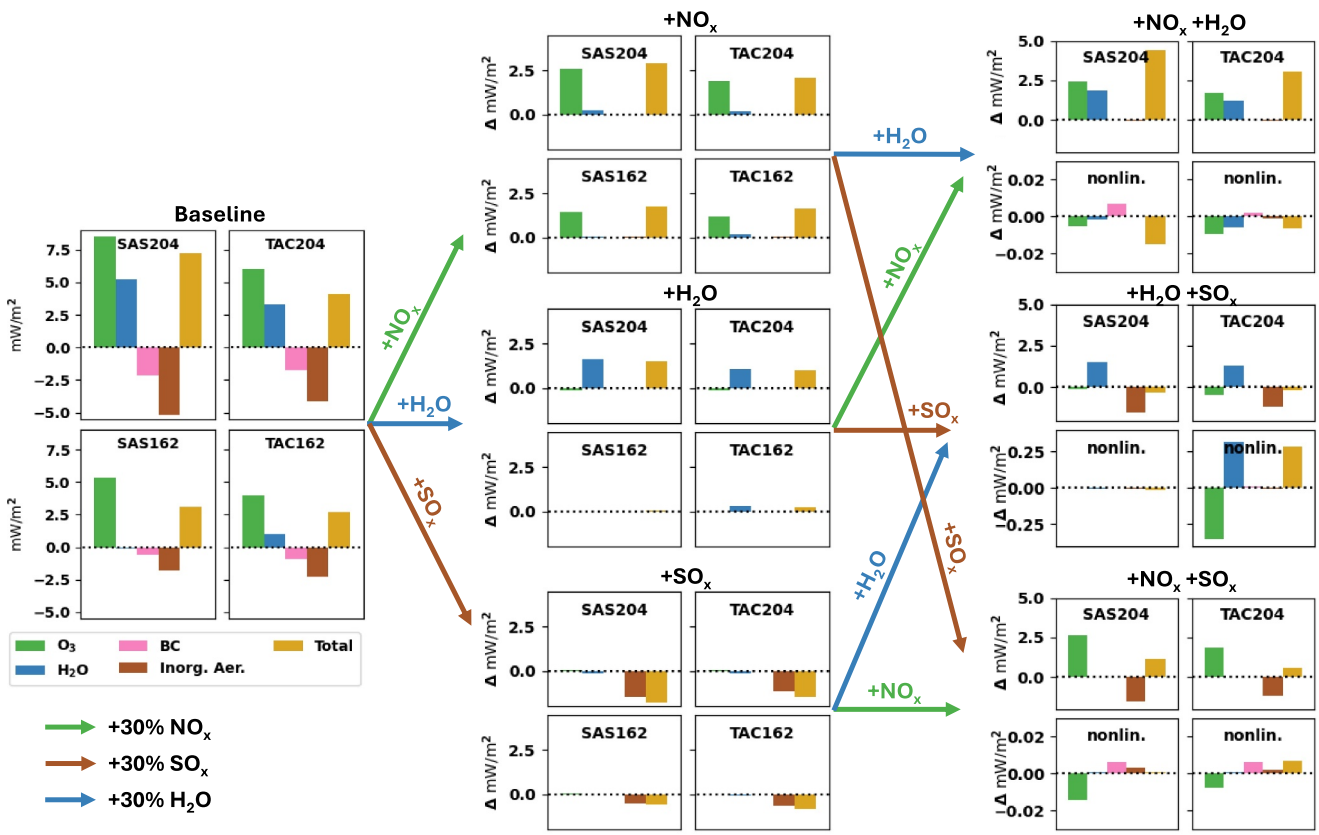

Figure 4. Overview of the impact on radiative forcing (RF) in mW/m^2 and the changes attributable to 30% increases in annual emissions of NO_x, SO_x, H_2O, and combinations thereof. On the left we show the change in global RF for the SAS204, TAC204, SAS162, and TAC162 scenarios. The middle column shows how the increase in NO_x, SO_x, and H_2O emissions alter these baseline impacts. The right column shows the second-order changes, with the fields for the SAS162 and TAC162 regions instead showing the non-linear component (nonlin.) of the second-order changes for the SAS204 and TAC204 regions. These are calculated as the difference between the combined change in emissions minus the individual contributions (e.g., the non-linearity of NO_x-H_2O is Δ RF (NO_x-H_2O) - (Δ RF (NO_x) + Δ RF (H_2O)). The colored arrows indicate the links between the emission scenarios.

Table 2
First- and Second-Order Sensitivities of the Global Mean Ozone Column and Global Mean Radiative Forcing (RF) to SST Emissions

	TAC		SAS			
Sensitivity	16.2 km	20.4 km	16.2 km	20.4 km	Units	Per
NO_x	2.09	−2.35	2.00	−4.29	mDU	Gg (NO_2) yr^{-1}
	0.04	0.05	0.04	0.07	mW/m^2	
SO_x	−21.97	−34.56	−16.77	−39.64	mDU	Gg (S) yr^{-1}
	−0.60	−1.02	−0.44	−1.25	mW/m^2	
H_2O	−1.42	−7.87	0.00	−11.19	mDU	Tg (H_2O) yr^{-1}
	0.08	0.33	0.00	0.50	mW/m^2	
FB	22.71	−72.97	25.55	−115.16	mDU	Gg yr^{-1}
	0.43	0.66	0.47	1.09	mW/m^2	
CO	0.20	–	–	–	mDU	Gg (HC) yr^{-1}
	−0.00	–	–	–	mW/m^2	
HC	0.03	–	–	–	mDU	Gg (CO) yr^{-1}
	0.00	–	–	–	mW/m^2	
NO_x + SO_x	–	92.43	–	85.40	µDU	Gg (NO_2) yr^{-1} Gg (S) yr^{-1}
	–	109.94	–	10.74	nW/m^2	
H_2O + SO_x	–	0.18	–	−0.06	µDU	Gg (H_2O) yr^{-1} Gg (S) yr^{-1}
	–	65.03	–	−2.72	nW/m^2	
H_2O + NO_x	–	0.02	–	0.02	µDU	Gg (H_2O) yr^{-1} Gg (NO_2) yr^{-1}
	–	−0.05	–	−0.11	nW/m^2	

Note. The FB entry shows the sensitivity to fuel burn mass estimated following Equation 1. For each species the sensitivity of the ozone column is shown above and RF below. The Unit column shows the unit of the sensitivity term, and the "Per" column shows the scaling per annual emission mass.

sensitivity to emissions originating from the SAS regions. Similar regional trends have been identified in earlier studies (Fritz et al., 2022; Gilmore et al., 2013; Speth et al., 2021; Zhang et al., 2023).

3.2. First-Order Ozone Sensitivities to Supersonic Aircraft Emissions

In Table 2 we show the sensitivities of the global ozone column and RF for the SAS and TAC regions. The sensitivity to fuel burn (S_{FB}) is calculated by scaling the individual sensitivities against the emission indices, following Equation 1. The sensitivities which we calculate depend on the background meteorology and the timeframe included in the averaging period, and we find that the use of different lengths and placements of the averaging window leads to changes in the calculated sensitivities (Text S4 Supporting Information S1). For the first-order sensitivities we find this can lead to fluctuations within 10% of the reported values, with greater effect on the second-order sensitivities. This is similar to fluctuations reported by Speth et al. (2021) (15%) and Eastham et al. (2022) (7%). The differences of our results with other studies are larger than this range, making it unlikely our results differ solely from the choice of background meteorology.

Figure 5 presents the sensitivities alongside estimated values from other studies. For the latter, if these sensitivities were not directly reported we estimated them using compatible emission scenarios from parametric analyses. A global mean ozone column of 300 DU was used to convert ozone impacts when reported in % ozone column changes. The sensitivities to individual emission species are discussed in subsequent sections.

3.2.1. Nitrogen Oxides

For NO_x emissions we find net-positive ozone sensitivities of 2.09 and 2.00 mDU/(Gg (NO_2) yr^{-1}) across both the SAS and TAC regions at an altitude of 16.2 km, indicating that NO_x-driven lower-stratospheric ozone increases exceed middle-stratospheric depletion. Some estimations from 2-dimensional models by Kawa et al. (1999) and an

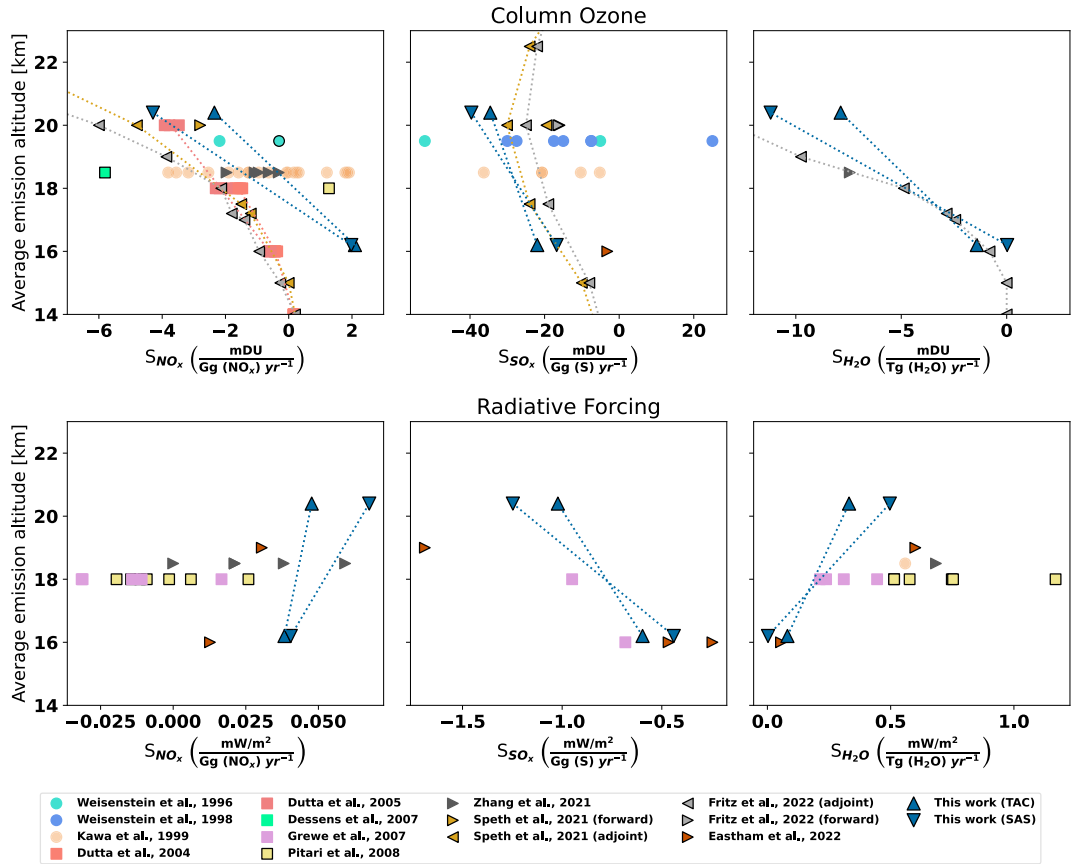

Figure 5. Sensitivities of ozone (top row) and radiative forcing (bottom row) to NO_x (left), SO_x (middle), and H_2O (right) emissions for a range of altitudes, including sensitivities reported in other studies or calculated from their data. Central altitudes are used for studies that reported bands of cruise altitudes (e.g., 17–20 yields 18.5). The literature cited in this figure is not a comprehensive overview, only works from which sensitivities can be inferred (e.g., from studies which evaluate multiple emission indices) are included.

inferred sensitivity from the ULAQ-CTM model used by Pitari et al. (2008) yield similar sensitivities, whereas observations from adjoint models and Dutta et al. report negative sensitivities at this altitude instead (Dutta et al., 2004, 2005; Fritz et al., 2022; Speth et al., 2021). Our O_3 depletion from NO_x may be reduced by the high availability of stratospheric sulfates from the inclusion of volcanic and SST SO_x emissions, the effect of which is not included in some studies (Fritz et al., 2022; Speth et al., 2021). This enhances the conversion of NO_x to nitric acid (HNO_3) through heterogeneous chemistry (Granier & Brasseur, 1992; Tie & Brasseur, 1995), reducing the strength of the NO_x perturbation that is transported to the upper stratosphere, and subsequently reducing NO_x driven ozone depletion. The decrease in NO_x sensitivity from increased sulfate availability is also noted in several earlier works (Kawa et al., 1999; Weisenstein et al., 1996, 1998). At 20.4 km altitude we find ozone sensitivities of −2.35 and −4.29 mDU/(Gg (NO_2) yr^{-1}) for the TAC and SAS regions respectively. This range of sensitivities agrees with values reported by Speth et al. (2021) and Dutta et al. (2004) at 20 km altitude; the former find a sensitivity of −2.8 mDU/(Gg (NO_2) yr^{-1}) using the forward GEOS-Chem model, which lies between our regional sensitivities at this altitude. Projections from a linear fit to our sensitivities also agree with sensitivities obtained from the work by Zhang et al. (2021b), the model ensemble used by Kawa et al. (1999), and estimations from Weisenstein et al. (1996). Compared to the adjoint GEOS-Chem estimates we find less ozone depletion across all altitudes, which may be due to its inability to capture non-linear interactions such as the ozone self-healing effect (Fritz et al., 2022; Speth et al., 2021).

The sensitivity of the global RF to NO_x emissions ranges from 0.04 mW/m^2/(Gg (NO_2) yr^{-1}) for both regions at 16.2 km to 0.07 and 0.05 mW/m^2/(Gg (NO_2) yr^{-1}) at 20.4 km for the respective SAS and TAC regions. Interpolating to 18.5 km altitude, our values lie within RF sensitivities inferred from Zhang et al. (2021b), but they are

higher than results from SCENIC scenarios (Grewe et al., 2007; Pitari et al., 2008). As shown in Figure 4, the RF sensitivity to NO_x is almost entirely driven by the changes in the O_3 distribution. We find that these changes lead to positive RF, which may be driven by the loss of high-altitude O_3 (Iglesias-Suarez et al., 2018; Lacis et al., 1990). This loss is enhanced for emissions from the SAS region, which may explain their higher RF sensitivity. Compared to the models used by Grewe et al. (2007) and Pitari et al. (2008), GEOS-Chem has a larger vertical domain (upper limit of 0.1 hPa vs. 10 hPa) and a higher vertical resolution, which may be why our results, and those of Eastham et al. (2022), capture more warming from upper-stratospheric O_3 loss.

3.2.2. Sulfur Oxides

Across all regions we find that the emission of SO_x leads to global ozone depletion. Per unit mass of emission, the depletion from SO_x is over 10 times stronger than that of NO_x, ranging from −16.77 to −39.64 mDU/(Gg (S) yr^{-1}) in the SAS region and −21.97 to −34.56 mDU/(Gg (S) yr^{-1}) in the TAC region. While the role of SO_x emissions has been extensively covered in earlier works (Eastham et al., 2022; Fritz et al., 2022; Kawa et al., 1999; Pitari et al., 2008; Speth et al., 2021; Weisenstein et al., 1996, 1998; Zhang et al., 2023), there are limited options for comparison of sensitivities, as only a few of these works evaluate ranges of SO_x emissions. Compared to forward-modeling results from Speth et al. (2021) and Fritz et al. (2022), we find up to double the sensitivity to SO_x emissions. Despite this higher value, our sensitivities lie within the range of sensitivities which can be inferred from the works of Kawa et al. (1999) and Weisenstein et al. (1996, 1998).

In terms of RF, SO_x emissions also have the highest impact per emission mass. At 16.2 km altitude we find sensitivities of −0.44 and −0.60 mW/m^2/(Gg (S) yr^{-1}) for the SAS and TAC regions. At 20.4 km altitude the sensitivities increase to −1.25 and −1.02 mW/m^2/(Gg (S) yr^{-1}). These sensitivities are entirely driven by increased cooling from inorganic aerosols. Even though the ozone column is very sensitive to SO_x emissions, there is negligible feedback on RF from O_3 when SO_x emissions increase (Figure 4). Compared to Eastham et al. (2022), we find similar RF sensitivities to SO_x at the 16.2 km altitude but lower sensitivities higher in the atmosphere. From work by Grewe et al. (2007) we can infer two sensitivities at emission altitudes of 16 and 18 km, with values of −0.683 and −0.950 mW/m^2/(Gg (S) yr^{-1}). These sensitivities are 33% and 20% stronger than our estimates at these altitudes, but they exhibit a similar slope over altitude.

Differences in the availability of ozone depleting substances may play a role in the higher sensitivity we observe (Austin & Wilson, 2010; Heckendorn et al., 2009; Muthers et al., 2015; Tie & Brasseur, 1995). In addition, we expect the quantity and distribution of emissions may also be a factor. We assess the sensitivity for an increase of 2.904 Gg (SO_x) yr^{-1} of annual SO_x emissions, which is considerably smaller than the annual SO_x emissions in scenarios used by the other works (Eastham et al., 2022; Kawa et al., 1999; Speth et al., 2021; Weisenstein et al., 1996). The limited availability of ozone-depleting substances may lead to saturation of the sulfur impact, leading studies with larger changes in annual SO_x emissions to find lower sensitivities per unit emission mass. This saturation would not be captured in the adjoint models (Fritz et al., 2022), which explains why our results are closer to the latter. The difference in ozone sensitivities may also be driven by differences in halogen availability (Austin & Wilson, 2010; Heckendorn et al., 2009; Muthers et al., 2015; Tie & Brasseur, 1995), and in the case of the comparison with results from Grewe et al. (2007), also differences in radiative transfer modeling and optical properties of sulfate aerosols.

Finally, we note that we do not capture the meteorological feedbacks of SO_x emissions on ozone chemistry. Studies have shown that the ozone impact of sulfates are influenced by the increases of lower-stratospheric temperatures and dynamics (Heckendorn et al., 2009; Muthers et al., 2015; Pitari et al., 2014), if this feedback is included the sensitivities to SO_x emissions may change considerably.

3.2.3. Water Vapor

For H_2O we calculate an ozone sensitivity of −1.42 mDU/(Tg (H_2O) yr^{-1}) at 16.2 km in the TAC region, which matches estimates from the adjoint model by Fritz et al. (2022). For the SAS region we find a smaller sensitivity of 21.43 μDU/(Tg (H_2O) yr^{-1}). At the altitude of 20.4 km we find stronger ozone sensitivities of −11.19 and −7.87 mDU/(Tg (H_2O) yr^{-1}) for the respective SAS and TAC regions. This is lower than the globally-averaged sensitivity profile from the adjoint model by Fritz et al. (2022), in part because their global average includes the

more sensitive southern hemisphere. For the 10° to 50°N range at 20 km they report a sensitivity of −5 mDU/(Tg (H_2O) yr^{-1}), which is lower than our calculated values for this latitude range.

Similar to the ozone sensitivities we find smaller RF sensitivities for the SAS region at the altitude of 16.2 km. We calculate a sensitivity of 2.53 μW/m^2/(Gg (H_2O) yr^{-1}), compared to 81.32 μW/m^2/(Gg (H_2O) yr^{-1}) for the TAC region. At 20.4 km altitude the global RF is more sensitive to SAS emissions with a sensitivity of 496.58 μW/m^2/(Gg (H_2O) yr^{-1}) compared to 331.30 μW/m^2/(Gg (H_2O) yr^{-1}) for the TAC region. Figure 4 shows that increases in H_2O emissions enhance warming from stratospheric H_2O, the magnitude of which is tied to the degree of stratospheric H_2O accumulation. Therefore the RF sensitivity to H_2O is inherently tied to the H_2O perturbation lifetime, which is also higher in the SAS region at this altitude (Table 1). At 16 km our results agree with those of Eastham et al. (2022) (55 μW/m^2/(Gg (H_2O) yr^{-1})), but at higher altitudes our sensitivities are lower than values from other works (Eastham et al., 2022; Fritz et al., 2022; Grewe et al., 2007; Pitari et al., 2008). This may be because we find considerable RF from O_3, which may reduce the potential of H_2O forcing. Furthermore, our sensitivities may also be lower because we consider regional emissions, which leads to more restricted transport of H_2O emissions compared to global supersonic emission inventories.

As previously discussed, GEOS-Chem uses fixed tropospheric mixing ratios for H_2O, allowing the troposphere to act as a sink for the stratospheric H_2O emissions. At the altitude of 16.2 km, the SAS162 region is frequently located in the model's troposphere, nullifying a large share of the H_2O emissions. We expect that this is the main reason for the low H_2O perturbation lifetime (0.13 months averaged) and subsequent sensitivities of emissions from this region. Models which include freely evolving tropospheric H_2O may find larger sensitivities from tropospheric-stratospheric transport of the emissions.

3.2.4. Carbon Monoxide and Hydrocarbons

We find that the emissions of CO and hydrocarbons lead to small increases in global ozone at 16.2 km in the TAC region, with respective sensitivities of 0.03 and 0.204 mDU/(Gg yr^{-1}). The RF sensitivity to these emissions is −1.244 and −0.265 μW/m^2/(Gg yr^{-1}) respectively. Given the small emission mass of these species their effects on O_3 and RF could be considered as negligible to reduce the complexity of surrogate models.

3.2.5. Combined Fuel Burn

We use the ozone and RF sensitivities to the emissions species to construct a response model following Equation 1, which estimates the ozone and RF sensitivity to the total fuel burn mass. The resulting sensitivity over altitude is shown in Figure 6 together with values from other studies. Between altitudes of 16 to 22 km, we estimate that the fuel burn sensitivity ranges between 32 and −168 mDU/(Tg yr^{-1}) for the SAS region, and 26 to −108 mDU/(Tg yr^{-1}) for the TAC region. At an altitude of 18.5 km our estimates are similar to sensitivities calculated from the assessments of the HSCT inventory by Kawa et al. (1999), as well as the more recent reassessment of this scenario using the WACCM4 model (Zhang et al., 2021a). Sensitivities from the adjoint model used by Fritz et al. (2022) indicate more ozone depletion instead. This is likely due to the previously discussed differences in NO_x sensitivities at 16.2 km.

The global RF sensitivities to fuel burn range from 0.43 to 1.33 mW/m^2/(Tg yr^{-1}) and 0.40 to 0.74 mW/m^2/(Tg yr^{-1}) for the SAS and TAC regions respectively. These values differ from sensitivities identified by Zhang et al. (2021b), which are composed of the forcing effects of H_2O and O_3. The foremost difference is that we include the cooling of aerosol emissions, which reduces warming RF, and by extension our sensitivity. We also note a difference in the altitude trend of the ozone response. Zhang et al. found that the RF from O_3 changes to net-cooling at emission altitudes over 19 km, with peak warming at emission altitudes of approximately 16 km, but our results show an increase over altitude instead. There are considerable differences with our study that may contribute to this. They evaluate this trend for a global emissions inventory with over 5 times the annual fuel burn of our regional emissions, and they do so in a future atmosphere without volcanic emissions (Zhang et al., 2021b). Together,this may lead to substantial differences in the ozone response, especially at higher emission altitudes.

Figures 6b and 6c show the speciated contribution to the global ozone response, which we evaluate using the same mathematical definition as Fritz et al. (2022). This contribution is calculated as the estimated absolute ozone column or RF response to individual components over the estimated response to the total increase in fuel burnt

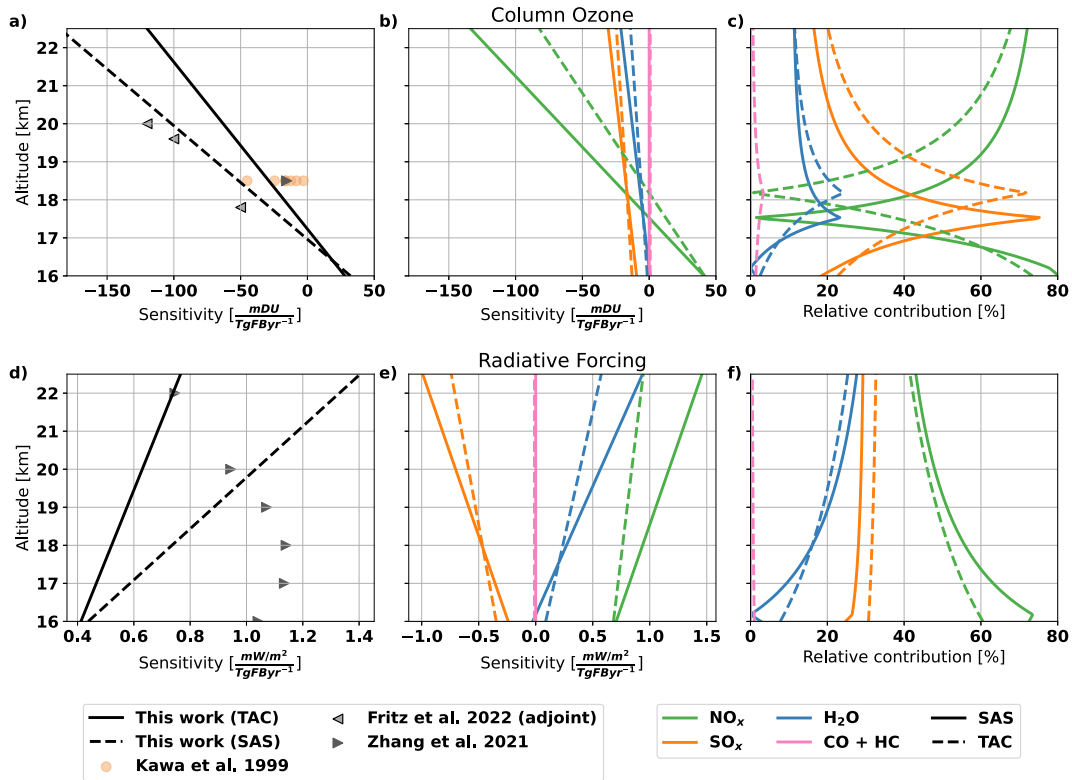

Figure 6. Fuel burn sensitivity of the global ozone column (top row) and global mean radiative forcing (RF) (bottom row). Solid and broken lines indicate results for the SAS and TAC regions respectively. (a) Estimated altitude-dependent sensitivity to mass of fuel burn. Markers indicate values from literature. Values from Fritz et al. (2022) are for the northern hemisphere. (b) Estimated component contributions of emission species to fuel burn sensitivity. (c) Estimated relative absolute contributions, derived by scaling sensitivities with emission indices. Panels (d–f) show the same as panels (a–c) but for the change in global mean RF.

$\left(\frac{|\Delta x S_x|}{\sum |\Delta x S_x|}\right)$. We use absolute values to accommodate comparisons for both positive or negative O_3 sensitivities. Like Fritz et al. (2022) and Speth et al. (2021), we find that NO_x emissions are the dominant driver of the ozone response and combined fuel-burn sensitivity, only exceeded by SO_x at the inflection point where the net response to increases in NO_x emissions is neutral. The inflection point of the response to NO_x emissions lies almost a km lower in the SAS region due to the enhancement of NO_x-driven ozone loss in this region. Furthermore, our estimates show that with increases in fuel burn NO_x emissions are the main driver of the RF impact, followed by the increased emission of SO_x and H_2O. Below 17 km altitude the estimated contribution of NO_x emissions exceeds 50%, and the relative contribution of H_2O increases with altitude. This agrees with other recent works which have highlighted that the effect of changes in the distribution of O_3 may be dominant in the RF impact of SST emissions (Eastham et al., 2022; Zhang et al., 2023). Similarly, our results suggest that the RF impact is predominantly driven by the emission of NO_x, rather than H_2O emissions which previously have been identified as the main driver of the climate footprint of SSTs (Grewe et al., 2007; Pitari et al., 2008).

Figure 6b shows that there is an inflection in mean change in the global ozone column at emission altitudes of 17.0 and 17.5 km for the TAC and SAS regions respectively. The inflection point does not indicate an altitude at which there is no change in the globally averaged ozone column, instead the regional increases balance out in a globally averaged metric. A similar value of 17.0 km was found by Zhang et al. (2021b). This altitude is lower than the inflection altitude which is calculated from the baseline scenarios (Table 1, 19.1 and 19.4 km for SAS and TAC). We hypothesize that this difference is indicative of a non-linear response of the sensitivities to stratospheric emissions. We find that NO_x emissions are the main driver of the ozone increases at lower altitudes, and the effectiveness of this mechanism decreases non-linearly with higher NO_x availability (Lin et al., 1988). As stratospheric NO_x emissions increase the lower-stratospheric production saturates, lowering the inflection altitude.

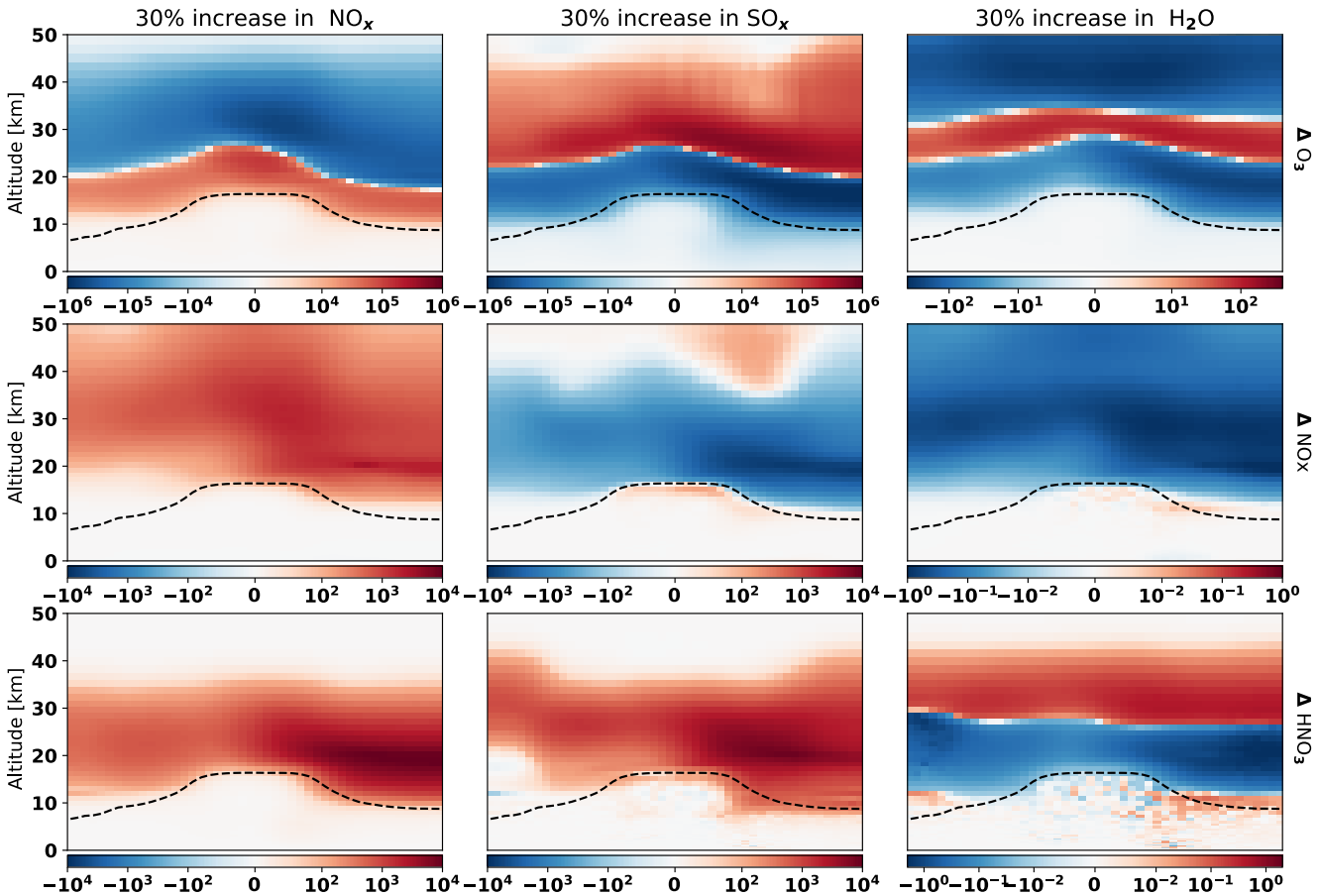

Figure 7. Mean change in mixing ratio of O_3, NO_x, and HNO_3 (top, middle, bottom) per Tg of increases in annual NO_x, SO_x, and H_2O (left, middle, right) emissions for the TAC204 perturbation scenario. Units are ppt Tg^{-1} yr^{-1}, expressed as emission mass of NO_2, S, and H_2O respectively.

3.3. Second-Order Ozone Interactions Between NO_x, SO_x, and H_2O

Cross-sensitivities between emission species stem from interactions between emissions over the course of the model integration. These interactions can be driven by indirect feedbacks and non-linearities in chemistry, and in case of NO_x, SO_x, and H_2O also from heterogeneous chemistry on sulfate aerosols. The effect of these interactions on stratospheric mixing ratios of O_3, NO_x, and HNO_3 to the increase of NO_x, SO_x, and H_2O emissions is shown in Figure 7.

Figure 7 shows that increases in annual SO_x emissions lead to increases of stratospheric HNO_3 of up to 8.8 ppb Tg^{-1} (S) yr^{-1}, as well as a decrease in stratospheric NO_x of up to −7.5 ppb Tg^{-1} (S) yr^{-1}. The reduction in stratospheric NO_x suppresses mid-stratospheric ozone depletion, leading to an increase in upper-stratospheric ozone of up to 553.4 ppb Tg^{-1} (S) yr^{-1}, which is offset by stronger ozone decreases in the lower-stratosphere from the increased availability of halogen radicals. Similarly, increases in H_2O emissions lead to small overall decreases in stratospheric NO_x and an increase in upper-stratospheric HNO_3, leading to a band of middle-stratospheric ozone increases. This band of O_3 increases reduces the warming effect of the O_3 displacement, which can also be seen in Figure 4.

The effect of these secondary interactions is captured in the second-order cross sensitivities. In Figure 8 we show the magnitude of these interactions on the ozone and RF impacts. Here, we evaluate the difference between a reduced order model accounting for cross-sensitivities ($\Delta O_3(X, Y) = \Delta X(S_x + \Delta YS_{xy}) + \Delta Y(S_y + \Delta XS_{xy})$) and one which assumes independent contributions ($\Delta O_3(X, Y) = \Delta XS_x + \Delta YS_y$) following the approach of Equation 1. For example, if both the annual NO_x and SO_x emissions increase by 1 Gg yr^{-1} in the TAC204 region, the latter (independent) model assumes the NO_x-attributable O_3 loss increases by −2.35 mDU. The former model

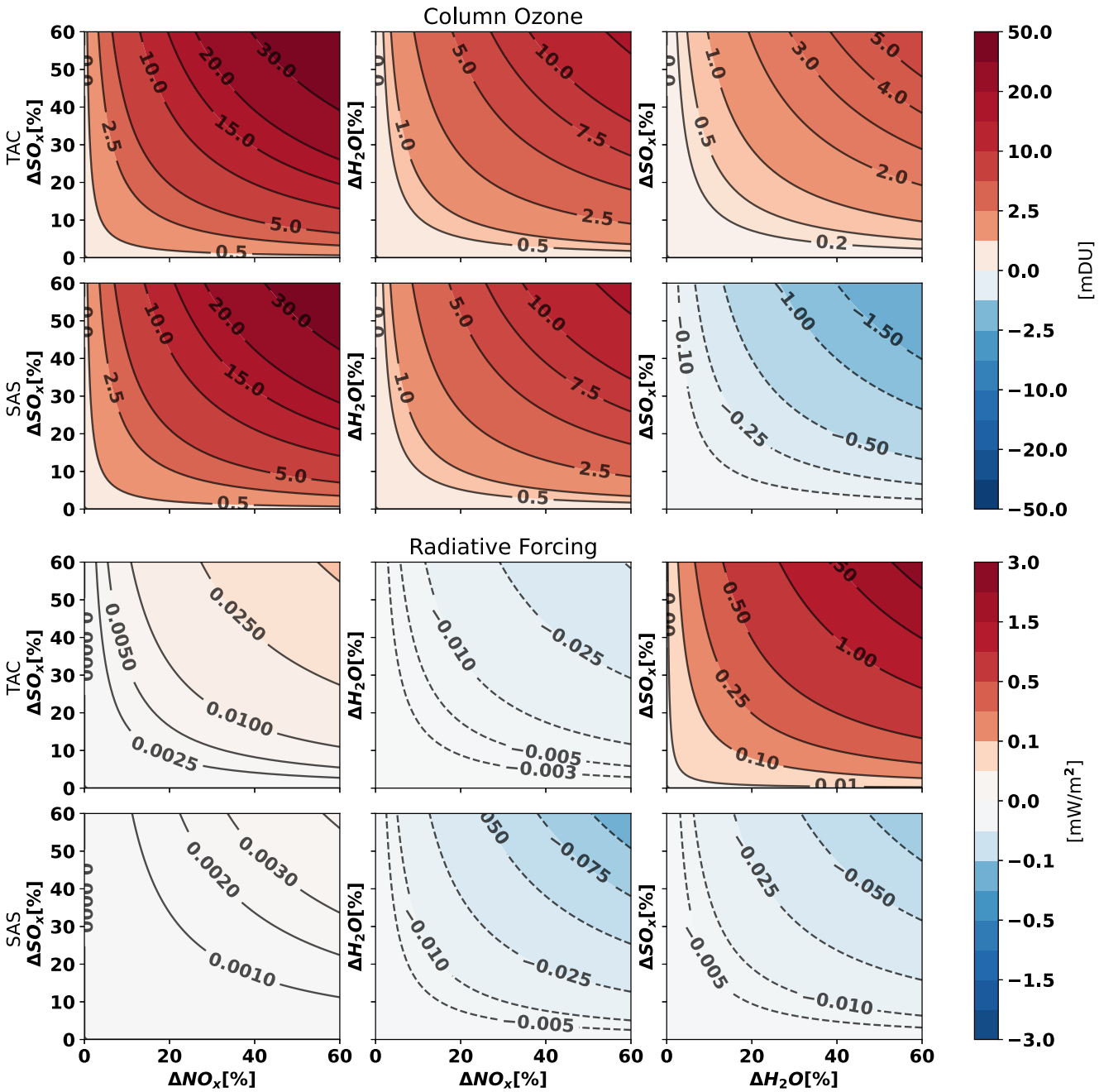

Figure 8. Magnitude of the cross-sensitivity terms for the global mean ozone column (rows 1 and 2) and global mean radiative forcing (rows 3 and 4) for the TAC and SAS regions (rows 1,3 and 2,4 respectively). The left column shows the magnitude of the interaction between increases in SO_x and NO_x emissions, the middle column H_2O and NO_x, and the right column SO_x and H_2O.

accounts for the decrease in NO_x sensitivity due to the increase in SO_x emissions, resulting in a value of −2.30 mDU instead. The difference, a relative increase of 0.05 mDU, is what we isolate and show in Figure 8.

Regarding the ozone impact, we find the strongest non-linear interactions between increases in SO_x and NO_x emissions. For the SAS and TAC regions we identify cross-sensitivities of 85.40 and 92.43 μDU/(Gg (S) yr^{-1} Gg (NO_2) yr^{-1}). The positive sign indicates that the non-linear interactions reduce global ozone loss. This likely driven by the increased heterogeneous conversion of NO_x to HNO_3 and subsequent suppression of upper-stratospheric ozone loss from NO_x cycles. This reduces O_3 loss across the entire northern hemisphere for both regions. Upon a simultaneous 30% increase in NO_x and SO_x emissions, we find that this interaction reduces global

ozone column depletion by 10.6 and 11.5 mDU for the SAS and TAC regions respectively. Relative to the total ozone column loss this represents reductions of 1.5% and 3.7%. The effect of interactions between H_2O and NO_x is smaller, with both regions having cross-sensitivities of 0.02 μDU/(Gg (H_2O) yr^{-1} Gg (NO_2) yr^{-1}), reducing ozone loss by 4.3 mDU, representing a difference of 0.6% and 1.3% for the respective SAS and TAC regions. The smallest non-linearity occurs between H_2O and SO_x emissions, both affecting the total column ozone impact by less than a percent. Unlike the other pairs, the interaction between SO_x and H_2O accelerates global ozone column loss instead for emissions from the SAS region, showing that the effect of second-order interactions may not be spatially homogeneous.

We find that non-linear interactions are of small effect on the global RF impact for most emission pairs. In the SAS regions the interactions between all emission pairs lead to non-linearities of less than 0.02 mW/m^2, which is less than 0.3% of the total RF impact. Similarly, for the TAC region we identify marginal non-linearities for interactions in all NO_x pairs, resulting in absolute changes of less than 0.1 mW/m^2, or smaller than 0.2%. The only exception is the H_2O and SO_x pair, where we find considerably stronger effects of their interactions. At a mutual 30% emissions increase interactions between these add a non-linear term of 0.29 mW/m^2, increasing the RF impact by 7.3%. Figure 4 shows that this non-linearity reduces warming from O_3 and cooling from black carbon, while increasing warming from H_2O. The source of this discrepancy lies in the complex ozone response to the interactions between the SO_x and H_2O emissions. As previously discussed, increases in H_2O or SO_x emissions lead to increases of upper-stratospheric O_3 (Figure 7). When both are emitted, upper-stratospheric O_3 loss is reduced, reducing warming from O_3 and increasing warming from H_2O instead. Isolating the non-linear O_3 term shows that a linear approach overestimates lower-stratospheric and tropospheric O_3 loss, while underestimating O_3 changes in the middle-upper stratosphere (Figure S13 in Supporting Information S1). This leads to a relatively large non-linear term in the RF of O_3, even though there is little effect on the global ozone column.

Across both regions the net non-linear term from chemical interactions between NO_x, SO_x, and H_2O emissions on global ozone is small. The most notable interaction is between NO_x-SO_x emissions, resulting in a non-linear reduction of the ozone impact by 3.7% at 30% increases to both annual emissions. IRF the strongest interaction occurs between H_2O and SO_x instead, increasing the RF by up to 7.3%. We find that the behavior of the NO_x-SO_x and NO_x-H_2O interactions is consistent across both regions, suggesting that latitude may not be as influential on second-order cross-sensitivities as it is on first-order sensitivities. The behavior of interactions between SO_x and H_2O emissions is not geographically consistent however, and for some emission areas this interaction may have non-negligible effects on the RF impact. Still, in many cases the effect of second-order interactions is small. The capacity to neglect latitudinal dependencies can simplify the implementation of cross-sensitivity effects in surrogate models, and our results suggest the effect of these interactions might also be left out entirely at a small cost in estimation accuracy.

4. Conclusions

With the rapid development of supersonic aviation technology and potential regulations, there is a growing need for surrogate models to rapidly evaluate the impacts of supersonic fleet emissions. Current methods utilize first-order approximations and sensitivities, but there is no knowledge about the importance of higher-order effects, such as from interactions between emission species. To assess the role of these second-order cross-sensitivities (e.g., a simultaneous increase to NO_x and SO_x emissions) in atmospheric response systems, we present a parametric study of first- and second-order sensitivities of the global ozone column and RF to supersonic aircraft emissions across two flight corridors. We evaluate the ozone impact of 26 emission scenarios over 10 years, covering cruise altitudes of 16.2, 18.3, and 20.4 km.

Across all scenarios, we find that the introduction of supersonic cruise emissions results in changes to the global ozone distribution and increases to global RF. Depending on the location and composition of the emissions, the global O_3 column changes by −0.94 to +0.40 DU. In all cases we find an increase to RF with values ranging between 1.81 and 11.69 mW m^{-2}. This forcing is primarily driven by the warming effect of changes in the distribution of O_3. Second to O_3 is the cooling effect of the accumulation of stratospheric sulfate and black carbon, and finally warming from stratospheric H_2O accumulation has the smallest effect on RF. We estimate that, upon an increase in fuel burn, the additional NO_x emissions are responsible for the majority of the impact on the global ozone column and RF, the latter driven by changes in the ozone distribution. This is followed by SO_x and H_2O.

Both CO and hydrocarbon emissions have negligible effects on ozone and RF. To reduce these impacts, we find that it would be most effective to reduce the emission altitude, followed by reducing NO_x emissions.

We show that supersonic aircraft emissions above the Arabian sea can lead to up to twice the ozone depletion and warming RF compared to equivalent emissions in the transatlantic flight corridor. This is related to this corridor's placement in the Brewer-Dobson circulation. The close proximity to the tropic pipes enhances transport of emissions to the upper-stratosphere, increasing their the stratospheric lifetime. This enhances NO_x-driven ozone depletion and the associated RF, while also increasing RF from H_2O emissions. It is likely that this increased sensitivity can be found across the extratropics, meaning that any supersonic flights over low latitudes will have enhanced impacts on global ozone and RF. Our results suggest this may best be mitigated by reducing the cruise altitude over these areas.

We also quantify, for the first time, the impact of second-order interactions between simultaneous increases in NO_x, SO_x, and H_2O emissions. We find that these interactions largely dampen global ozone loss, albeit at a small scale. Above the transatlantic flight corridor the interaction between SO_x and NO_x emissions is strongest, dampening ozone loss by 3.7%, followed by reductions of 1.3% and 0.5% from the interactions between H_2O-NO_x and H_2O-SO_x. Above the Arabian sea, the second-order sensitivities between NO_x-SO_x and NO_x-H_2O only deviate slightly from the transatlantic values. Given the higher ozone depletion from emissions in this region, the relative reduction in ozone depletion from these interactions is reduced to 1.5% and 0.6% respectively. In the second-order sensitivities of RF we identify different behavior, most of the interactions between NO_x, SO_x, and H_2O emissions result in negligible non-linear terms (<0.3%), with the exception of H_2O and SO_x in the TAC emissions region. In this case interactions between H_2O and SO_x emissions enhance global RF by 7.3%.

The small magnitude of most of the second-order interactions between NO_x, SO_x, and H_2O emissions may suggest that their effect could be neglected to simplify response models at a small cost in accuracy. This could extend our capacity to use first-order models to estimate the effects of complex changes in emissions composition, such as from the use of different fuel blends or alternative fuel types. However, we note that more research into these second-order interactions is needed as we expect that their behavior may differ at lower altitudes. They may also play a bigger role in the southern hemisphere or in different CTMs, especially if these can capture meteorological feedbacks (see also Pletzer and Grewe (2024)).

Data Availability Statement

This work used data from ESA's TROPOMI instrument database (ESA, 2019b; ESA, 2019c). The atmospheric models used meteorological data from the MERRA-2 reanalysis (Gelaro et al., 2017), anthropogenic emissions from CEDSv2 (O'Rourke et al., 2021), aviation emissions from openAVEM (Quadros et al., 2022), and a collection of specialized emission inventories (Giglio et al., 2013; Liang et al., 2010; Murray, 2016; Murray et al., 2012; Ordóñez et al., 2012; Ott et al., 2010; Philip et al., 2017; Tzompa-Sosa et al., 2017; Xiao et al., 2008). Results of this work were generated using GCC v13.3.1 (The International GEOS-Chem User Community, 2021), and GEOS-Chem High performance v14.3.1 (The International GEOS-Chem User Community, 2024) was used for the assessment of RF. For more information see https://geoschem.github.io/. Processing and visualisation of the results was done in Python 3.11.6 with support of the Matplotlib (The Matplotlib Development Team, 2023) (https://matplotlib.org/), Dask (Dask Development Team, 2023) (https://www.dask.org/), and Xarray libraries (Hoyer et al., 2023) (https://xarray.dev/). The data supporting this work's results is published in open access and can be accessed through https://doi.org/10.4121/d5947a0d-f34d-400b-87de-46ebda16ec44.

Acknowledgments
This work was funded as a part of the MORE and LESS (MDO and REgulations for Low-boom Environmentally Sustainable Supersonic aviation) research project as a part of the Horizon 2020 cycle (grant agreement 101006856, https://doi.org/10.3030/101006856). This work made use of the Dutch national e-infrastructure and supercomputer with the support of the SURF Cooperative using grants no. EINF-1504, EINF-3690, and EINF-5945. Additionally, we acknowledge the use of computational resources of the DelftBlue supercomputer, provided by Delft High Performance Computing Centre (https://www.tudelft.nl/dhpc).

References

Andrews, A. E., Boering, K. A., Daube, B. C., Wofsy, S. C., Loewenstein, M., Jost, H., et al. (2001). Mean ages of stratospheric air derived from in situ observations of CO_2, CH_4, and N_2O. *Journal of Geophysical Research*, *106*(D23), 32295–32314. https://doi.org/10.1029/2001JD000465

Austin, J., & Wilson, R. J. (2010). Sensitivity of polar ozone to sea surface temperatures and halogen amounts. *Journal of Geophysical Research*, *115*(D18). https://doi.org/10.1029/2009JD013292

Bian, H., & Prather, M. J. (2002). Fast-J2: Accurate simulation of stratospheric photolysis in global chemical models. *Journal of Atmospheric Chemistry*, *41*(3), 281–296. https://doi.org/10.1023/a:1014980619462

Brasseur, G., & Granier, C. (1992). Mount pinatubo aerosols, chlorofluorocarbons, and ozone depletion. *Science*, *257*(5074), 1239–1242. https://doi.org/10.1126/science.257.5074.1239

Butchart, N. (2014). The Brewer-Dobson circulation. *Reviews of Geophysics*, *52*(2), 157–184. https://doi.org/10.1002/2013RG000448

Chabrillat, S., Vigouroux, C., Christophe, Y., Engel, A., Errera, Q., Minganti, D., et al. (2018). Comparison of mean age of air in five reanalyses using the BASCOE transport model. *Atmospheric Chemistry and Physics*, *18*(19), 14715–14735. https://doi.org/10.5194/acp-18-14715-2018

Danilin, M. Y., Rodriguez, J. M., Ko, M. K. W., Weisenstein, D. K., Brown, R. C., Miake-Lye, R. C., & Anderson, M. R. (1997). Aerosol particle evolution in an aircraft wake: Implications for the high-speed civil transport fleet impact on ozone. *Journal of Geophysical Research*, *102*(D17), 21–453. https://doi.org/10.1029/97JD01483

Dask Development Team. (2023). Dask; Library for dynamic task scheduling [Software]. Retrieved from http://dask.pydata.org

de, F., Forster, P. M., & Shine, K. P. (1997). Radiative forcing and temperature trends from stratospheric ozone changes. *Journal of Geophysical Research*, *102*(D9), 10841–10855. https://doi.org/10.1029/96JD03510

Dedoussi, I. C., Henze, D. K., Eastham, S. D., Speth, R. L., & Barrett, S. R. H. (2024). Development of the adjoint of the unified tropospheric–stratospheric chemistry extension (UCX) in GEOS-Chem adjoint v36. *Geoscientific Model Development*, *17*(14), 5689–5703. https://doi.org/10.5194/gmd-17-5689-2024

Dube, K. (2023). Emerging from the COVID-19 pandemic: Aviation recovery, challenges and opportunities. *Aerospace*, *10*(1), 19. https://doi.org/10.3390/aerospace10010019

Dutta, M., Patten, K., & Wuebbles, D. (2004). Parametric analyses of potential effects on stratospheric and tropospheric ozone chemistry by a fleet of supersonic business jets projected in a 2020 atmosphere. *(No. NASA/CR-2004-213306)*.

Dutta, M., Patten, K. O., & Wuebbles, D. J. (2005). In *Parametric analyses of potential effects on upper tropospheric/lower stratospheric ozone chemistry by a future fleet of high speed civil transport (HSCT) type aircraft* (Vol. 36).

Eastham, S. D., Fritz, T., Sanz-Morère, I., Prashanth, P., Allroggen, F., Prinn, R. G., et al. (2022). Impacts of a near-future supersonic aircraft fleet on atmospheric composition and climate. *Environmental Sciences: Atmosphere*, *2*(3), 388–403. https://doi.org/10.1039/d1ea00081k

Eastham, S. D., Weisenstein, D. K., & Barrett, S. R. H. (2014). Development and evaluation of the unified tropospheric–stratospheric chemistry extension (UCX) for the global chemistry-transport model GEOS-Chem. *Atmospheric Environment*, *89*, 52–63. https://doi.org/10.1016/j.atmosenv.2014.02.001

Eastham, S. D., Weisenstein, D. K., Keith, D. W., & Barrett, S. R. H. (2018). Quantifying the impact of sulfate geoengineering on mortality from air quality and UV-B exposure. *Atmospheric Environment*, *187*, 424–434. https://doi.org/10.1016/j.atmosenv.2018.05.047

ESA. (2019a). Sentinel-5P TROPOMI carbon monoxide CO column 1-orbit L2 5. 5km x 7km [Dataset]. https://doi.org/10.5270/S5P-1hkp7rp

ESA. (2019b). Sentinel-5P TROPOMI total ozone column 1-orbit L2 5.5km x 3. 5km [Dataset]. https://doi.org/10.5270/S5P-fqouvyz

ESA. (2019c). Sentinel-5P TROPOMI tropospheric NO2 1-orbit L2 5.5km x 3. 5km [Dataset]. https://doi.org/10.5270/S5P-s4ljg54

Fritz, T. M., Dedoussi, I. C., Eastham, S. D., Speth, R. L., Henze, D. K., & Barrett, S. R. H. (2022). Identifying the ozone-neutral aircraft cruise altitude. *Atmospheric Environment*, *276*, 119057. https://doi.org/10.1016/j.atmosenv.2022.119057

Gelaro, R., McCarty, W., Suárez, M. J., Todling, R., Molod, A., Takacs, L., et al. (2017). The modern-era retrospective analysis for research and applications, version 2 (MERRA-2) [Dataset]. *Journal of Climate*, *30*(14), 5419–5454. https://doi.org/10.1175/JCLI-D-16-0758.1

Giglio, L., Randerson, J. T., & van der Werf, G. R. (2013). Analysis of daily, monthly, and annual burned area using the fourth-generation global fire emissions database (GFED4) [Dataset]. *Journal of Geophysical Research: Biogeosciences*, *118*(1), 317–328. https://doi.org/10.1002/jgrg.20042

Gilmore, C. K., Barrett, S. R. H., Koo, J., & Wang, Q. (2013). Temporal and spatial variability in the aviation NOx -related O3 impact. *Environmental Research Letters*, *8*(3), 034027. https://doi.org/10.1088/1748-9326/8/3/034027

Granier, C., & Brasseur, G. (1992). Impact of heterogeneous chemistry on model predictions of ozone changes. *Journal of Geophysical Research*, *97*(D16), 18015–18033. https://doi.org/10.1029/92JD02021

Grewe, V., Plohr, M., Cerino, G., Di Muzio, M., Deremaux, Y., Galerneau, M., et al. (2010). Estimates of the climate impact of future small-scale supersonic transport aircraft-results from the HISAC EU-project. Tech. Rep.), *114*(1153), 199–206. https://doi.org/10.1017/s000192400000364x

Grewe, V., Stenke, A., Plohr, M., & Korovkin, V. D. (2010). Climate functions for the use in multi-disciplinary optimisation in the pre-design of supersonic business jet. *Aeronautical Journal*, *114*(1154), 259–269. https://doi.org/10.1017/s0001924000003705

Grewe, V., Stenke, A., Ponater, M., Sausen, R., Pitari, G., Iachetti, D., et al. (2007). Climate impact of supersonic air traffic: An approach to optimize a potential future supersonic fleet – Results from the EU-project SCENIC. *Atmospheric Chemistry and Physics*, *7*(19), 5129–5145. https://doi.org/10.5194/acp-7-5129-2007

Heald, C. L., Ridley, D. A., Kroll, J. H., Barrett, S. R. H., Cady-Pereira, K. E., Alvarado, M. J., & Holmes, C. D. (2014). Contrasting the direct radiative effect and direct radiative forcing of aerosols. *Atmospheric Chemistry and Physics*, *14*(11), 5513–5527. https://doi.org/10.5194/acp-14-5513-2014

Heckendorn, P., Weisenstein, D., Fueglistaler, S., Luo, B. P., Rozanov, E., Schraner, M., et al. (2009). The impact of geoengineering aerosols on stratospheric temperature and ozone. *Environmental Research Letters*, *4*(4), 045108. https://doi.org/10.1088/1748-9326/4/4/045108

Hofmann, D. J., & Solomon, S. (1989). Ozone destruction through heterogeneous chemistry following the eruption of El Chichón. *Journal of Geophysical Research*, *94*(D4), 5029–5041. https://doi.org/10.1029/JD094iD04p05029

Hoyer, S., Roos, M., Joseph, H., Magin, J., Cherian, D., Fitzgerald, C., et al. (2023). Xarray 2023.9.0 [Software]. *Zenodo*. https://doi.org/10.5281/zenodo.8379187

ICAO. (2017). Annex 16 - environmental protection - volume II - aircraft engine emissions. *AIAA Journal*.

Iglesias-Suarez, F., Kinnison, D. E., Rap, A., Maycock, A. C., Wild, O., & Young, P. J. (2018). Key drivers of ozone change and its radiative forcing over the 21st century. *Atmospheric Chemistry and Physics*, *18*(9), 6121–6139. https://doi.org/10.5194/acp-18-6121-2018

Johnston, H. (1971). Reduction of stratospheric ozone by nitrogen oxide catalysts from supersonic transport exhaust. *Science*, *173*(3996), 517–522. https://doi.org/10.1126/science.173.3996.517

Kawa, S. R., Anderson, J. G., Baughcum, S. L., Brock, C. A., Brune, W. H., Cohen, R. C., et al. (1999). Assessment of the effects of high-speed aircraft in the stratosphere.

Kinnison, D., Brasseur, G. P., Baughcum, S. L., Zhang, J., & Wuebbles, D. (2020). The impact on the ozone layer of a potential fleet of civil hypersonic aircraft. *Earth's Future*, *8*(10). https://doi.org/10.1029/2020ef001626

Krishna-Pillai Sukumara-Pillai, K., Bala, G., Cao, L., Duan, L., & Caldeira, K. (2019). Climate system response to stratospheric sulfate aerosols: sensitivity to altitude of aerosol layer (preprint). *Dynamics of the Earth System: Concepts*. https://doi.org/10.5194/esd-2019-21

Lacis, A. A., Wuebbles, D. J., & Logan, J. A. (1990). Radiative forcing of climate by changes in the vertical distribution of ozone. *Journal of Geophysical Research*, *95*(D7), 9971–9981. https://doi.org/10.1029/JD095iD07p09971

Lary, D. J. (1997). Catalytic destruction of stratospheric ozone. *Journal of Geophysical Research*, *102*(D17), 21515–21526. https://doi.org/10.1029/97jd00912

Lee, D. S., Fahey, D. W., Skowron, A., Allen, M. R., Burkhardt, U., Chen, Q., et al. (2021). The contribution of global aviation to anthropogenic climate forcing for 2000 to 2018. *Atmospheric Environment*, *244*, 117834. https://doi.org/10.1016/j.atmosenv.2020.117834

Liang, Q., Stolarski, R. S., Kawa, S. R., Nielsen, J. E., Douglass, A. R., Rodriguez, J. M., et al. (2010). Finding the missing stratospheric Br_y: A global modeling study of $CHBr_3$ and CH_2Br_2 [Dataset]. *Atmospheric Chemistry and Physics*, *10*(5), 2269–2286. https://doi.org/10.5194/acp-10-2269-2010

Lin, X., Trainer, M., & Liu, S. C. (1988). On the nonlinearity of the tropospheric ozone production. *Journal of Geophysical Research*, *93*(D12), 15879–15888. https://doi.org/10.1029/JD093iD12p15879

Maloney, C. M., Portmann, R. W., Ross, M. N., & Rosenlof, K. H. (2022). The climate and ozone impacts of black carbon emissions from global rocket launches. *Journal of Geophysical Research: Atmospheres*, *127*(12). https://doi.org/10.1029/2021JD036373

Maruhashi, J., Grewe, V., Frömming, C., Jöckel, P., & Dedoussi, I. C. (2022). Transport patterns of global aviation NO_x and their short-term O_3 radiative forcing - a machine learning approach. *Atmospheric Chemistry and Physics Discussions*, 1–40. https://doi.org/10.5194/acp-2022-348

Matthes, S., Lee, D. S., De Leon, R. R., Lim, L., Owen, B., Skowron, A., et al. (2022). Review: The effects of supersonic aviation on ozone and climate. *Aerospace*, *9*(1), 41. https://doi.org/10.3390/aerospace9010041

McKenzie, R., Aucamp, P. J., Bais, A. F., Björn, L. O., Ilyas, M., & Madronich, S. (2015). Ozone depletion and climate change: Impacts on UV radiation. *Photochemical and Photobiological Sciences*, *10*(2), 182–198. https://doi.org/10.1039/c0pp90034f

Murray, L. T. (2016). Lightning nox and impacts on air quality [Dataset]. *Current Pollution Reports*, *2*(2), 115–133. https://doi.org/10.1007/s40726-016-0031-7

Murray, L. T., Jacob, D. J., Logan, J. A., Hudman, R. C., & Koshak, W. J. (2012). Optimized regional and interannual variability of lightning in a global chemical transport model constrained by LIS/OTD satellite data [Dataset]. *Journal of Geophysical Research*, *117*(D20). https://doi.org/10.1029/2012jd017934

Muthers, S., Arfeuille, F. X., Raible, C. C., & Rozanov, E. (2015). The impacts of volcanic aerosol on stratospheric ozone and the Northern Hemisphere polar vortex: Separating radiative-dynamical changes from direct effects due to enhanced aerosol heterogeneous chemistry. *Atmospheric Chemistry and Physics*, *15*(20), 11461–11476. https://doi.org/10.5194/acp-15-11461-2015

Ordóñez, C., Lamarque, J. F., Tilmes, S., Kinnison, D. E., Atlas, E. L., Blake, D. R., et al. (2012). Bromine and iodine chemistry in a global chemistry-climate model: Description and evaluation of very short-lived oceanic sources [Dataset]. *Atmospheric Chemistry and Physics*, *12*(3), 1423–1447. https://doi.org/10.5194/acp-12-1423-2012

O'Rourke, P. R., Smith, S. J., Mott, A., Ahsan, H., McDuffie, E. E., Crippa, M., et al. (2021). CEDS v_2021_02_05 release emission data [Dataset]. *Zenodo*. https://doi.org/10.5281/zenodo.4509372

Ott, E., Pickering, E., Stenchikov, L., Allen, J., DeCaria, J., Ridley, A., et al. (2010). Production of lightning NOx and its vertical distribution calculated from three-dimensional cloud-scale chemical transport model simulations [Dataset]. *Journal of Geophysical Research*, *115*(D4). https://doi.org/10.1029/2009JD011880

Penner, J. E., Lister, D., Griggs, D. J., Dokken, D. J., & McFarland, M. (1999). *Aviation and the global atmosphere: A special report of the intergovernmental panel on climate change*. Cambridge University Press.

Philip, S., Martin, R. V., Snider, G., Weagle, C. L., van Donkelaar, A., Brauer, M., et al. (2017). Anthropogenic fugitive, combustion and industrial dust is a significant, underrepresented fine particulate matter source in global atmospheric models [Dataset]. *Environmental Research Letters*, *12*(4). 044018. https://doi.org/10.1088/1748-9326/aa65a4

Pitari, G., Aquila, V., Kravitz, B., Robock, A., Watanabe, S., Cionni, I., et al. (2014). Stratospheric ozone response to sulfate geoengineering: Results from the geoengineering model intercomparison project (GeoMIP). *Journal of Geophysical Research*, *119*(5), 2629–2653. https://doi.org/10.1002/2013jd020566

Pitari, G., Iachetti, D., Mancini, E., Montanaro, V., De Luca, N., Marizy, C., et al. (2008). Radiative forcing from particle emissions by future supersonic aircraft. *Atmospheric Chemistry and Physics*, *8*(14), 4069–4084. https://doi.org/10.5194/acp-8-4069-2008

Pletzer, J., & Grewe, V. (2024). Sensitivities of atmospheric composition and climate to altitude and latitude of hypersonic aircraft emissions. *Atmospheric Chemistry and Physics*, *24*(3), 1743–1775. https://doi.org/10.5194/acp-24-1743-2024

Pletzer, J., Hauglustaine, D., Cohen, Y., Jöckel, P., & Grewe, V. (2022). The climate impact of hydrogen-powered hypersonic transport. *Atmospheric Chemistry and Physics*, *22*(21), 14323–14354. https://doi.org/10.5194/acp-22-14323-2022

Quadros, F. D. A., Snellen, M., & Dedoussi, I. C. (2020). Regional sensitivities of air quality and human health impacts to aviation emissions. *Environmental Research Letters*, *15*(10), 105013. https://doi.org/10.1088/1748-9326/abb2c5

Quadros, F. D. A., Snellen, M., Sun, J., & Dedoussi, I. C. (2022). Global civil aviation emissions estimates for 2017–2020 using ADS-B data [Dataset]. *Journal of Aircraft*, *59*(6), 1–11. https://doi.org/10.2514/1.C036763

Simone, N. W., Stettler, M. E. J., & Barrett, S. R. H. (2013). Rapid estimation of global civil aviation emissions with uncertainty quantification. *Transportation Research Part D: Transport and Environment*, *25*, 33–41. https://doi.org/10.1016/j.trd.2013.07.001

Solomon, S. (1999). *Stratospheric ozone depletion: A review of concepts and history*. Blackwell Publishing Ltd.

Speth, R. L., Eastham, S. D., Fritz, T. M., Sanz-Morére, I., Agarwal, A., Prashanth, P., et al. (2021). Global environmental impact of supersonic cruise aircraft in the stratosphere. Tech. Rep.

The International GEOS-Chem User Community. (2021). Geoschem/GCClassic: GEOS-chem 13.3.1 [Software]. *Zenodo*. https://doi.org/10.5281/zenodo.5703364

The International GEOS-Chem User Community. (2024). Geoschem/GCHP: Gchp 14.3.1 [Software]. *Zenodo*. https://doi.org/10.5281/zenodo.10909030

The Matplotlib Development Team. (2023). Matplotlib: Visualization with Python [Software]. *Zenodo*. https://doi.org/10.5281/zenodo.8347255

Tie, X., & Brasseur, G. (1995). The response of stratospheric ozone to volcanic eruptions: Sensitivity to atmospheric chlorine loading. *Geophysical Research Letters*, *22*(22), 3035–3038. https://doi.org/10.1029/95GL03057

Tuck, A. F. (2021). Perspective on aircraft in the stratosphere: 50 years from COMESA through the ozone hole to climate. *Quarterly Journal of the Royal Meteorological Society*, *147*(735), 713–727. https://doi.org/10.1002/qj.3958

Tzompa-Sosa, Z. A., Mahieu, E., Franco, B., Keller, C. A., Turner, A. J., Helmig, D., et al. (2017). Revisiting global fossil fuel and biofuel emissions of ethane [Dataset]. *Journal of Geophysical Research: Atmospheres*, *122*(4), 2493–2512. https://doi.org/10.1002/2016jd025767

Weisenstein, D. K., Ko, M. K. W., Dyominov, I. G., Pitari, G., Ricciardulli, L., Visconti, G., & Bekki, S. (1998). The effects of sulfur emissions from HSCT aircraft: A 2-D model intercomparison. *Journal of Geophysical Research*, *103*(D1), 1527–1547. https://doi.org/10.1029/97JD02930

Weisenstein, D. K., Ko, M. K. W., Sze, N.-D., & Rodriguez, J. M. (1996). Potential impact of SO2 emissions from stratospheric aircraft on ozone. *Geophysical Research Letters*, *23*(2), 161–164. https://doi.org/10.1029/95GL03781

Weisenstein, D. K., Visioni, D., Franke, H., Niemeier, U., Vattioni, S., Chiodo, G., et al. (2021). A model intercomparison of stratospheric solar geoengineering by accumulation-mode sulfate aerosols. https://doi.org/10.5194/acp-2021-569

Xiao, Y., Logan, J. A., Jacob, D. J., Hudman, R. C., Yantosca, R., & Blake, D. R. (2008). Global budget of ethane and regional constraints on US sources [Dataset]. *Journal of Geophysical Research*, *113*(D21). https://doi.org/10.1029/2007jd009415

Zhang, J., Wuebbles, D., Kinnison, D., & Baughcum, S. L. (2021a). Potential impacts of supersonic aircraft emissions on ozone and resulting forcing on climate: An update on historical analysis. *Journal of Geophysical Research: Atmospheres*, *126*(6). https://doi.org/10.1029/2020JD034130

Zhang, J., Wuebbles, D., Kinnison, D., & Baughcum, S. L. (2021b). Stratospheric ozone and climate forcing sensitivity to cruise altitudes for fleets of potential supersonic transport aircraft. *Journal of Geophysical Research: Atmospheres*, *126*(16). https://doi.org/10.1029/2021jd034971

Zhang, J., Wuebbles, D., Pfaender, J. H., Kinnison, D., & Davis, N. (2023). Potential impacts on ozone and climate from a proposed fleet of supersonic aircraft. *Earth's Future*, *11*(4), e2022EF003409. https://doi.org/10.1029/2022EF003409